Department of Theoretical Physics and Astrophysics

Faculty of Science
Masaryk University

Ph.D. Dissertation

Tomáš Henych

Excitation of asteroid rotations through impacts

Supervisor: Mgr. Petr Pravec, Dr.

Brno 2013

Bibliographic Entry

Bibliografický záznam

Abstract

Most asteroids are found to be in principal axis rotation states. There is, however, a group of asteroids, called *tumblers*, which are in an excited state of rotation, i.e., freely precessing. This is indicated by their complex, two-periodic, lightcurves and also by radar measurements of the first confirmed and also the best described tumbler, 4179 Toutatis.

A damping of the excited rotation is rather fast in most asteroids which explains why we observe most of them in a basic rotation state. A question arises on how were the asteroids excited. There are two major mechanisms to explain this, collisions and a torque related to Yarkovsky–O'Keefe–Radzievskii–Paddack (YORP) effect.

In the thesis we describe an analytical model we constructed to verify the plausibility of the collisional mechanism of the excitation of asteroid rotation. The main features of the model are the scaling laws used for calculation of the impact crater dimensions and the angular momentum transfer efficiency based on laboratory impact experiments. After the collision, a rotational lightcurve is generated for the simulated asteroid and we judge if the tumbling is detectable by the standard photometric analysis.

We found that large subcatastrophic collisions are a plausible mechanism to excite rotations of small slowly rotating asteroids. The rotational axis misalignment is used as a measure of tumbling magnitude. Tumbling begins to be detectable for the misalignment angle larger than $\sim 15°$ with high accuracy data.

We also found that the result of a collision can be simply described by the ratio of the orbital angular momentum (mainly carried by the projectile) and the rotational angular momentum of the target. We derived a relation between this ratio and the rotational axis misalignment.

In addition, we compared the specific impact energy of the collision to the threshold energy which would already cause a serious damage to the asteroid. We found that asteroids as small as $\sim 100\,\mathrm{m}$ can have excited rotation by collision without being damaged. Finally, we discuss our results and describe further work to be done to understand the processes that excite asteroid rotations.

Abstrakt

Podle fotometrických pozorování rotuje většina planetek kolem své nejkratší hlavní osy. Několik desítek dnes známých planetek, kterým se říká *tumbleři*, mají ale excitovanou rotaci. Soudíme tak podle jejich složitých dvouperiodických křivek a také radarových pozorování planetky 4179 Toutatis, která je prvním potvrzeným a zároveň nejlépe popsaným tumblerem.

Disipace energie vede k útlumu excitované rotace a návratu do základního rotačního stavu. Časová škála tohoto procesu je pro většinu planetek poměrně krátká. Je tedy logické se ptát, jakým způsobem může být rotace planetek excitována. Hlavní procesy ovlivňující rotaci planetek jsou jejich vzájemné srážky a moment síly spojený s Yarkovsky–O'Keefe–Radzievskii–Paddack (YORP) efektem.

V této dizertaci popíšeme analytický model, kterým ověřujeme, jestli mohou být srážky zodpovědné za excitaci rotace. Model využívá škálovací zákony pro výpočet velikosti impaktních kráterů a také účinnost přenosu momentu hybnosti mezi srážejícími se planetkami. Po srážce spočteme světelnou křivku planetky s kráterem a standardní fotometrickou analýzou posoudíme, jestli planetka viditelně preceduje.

Zjistili jsme, že srážky mohou excitovat rotaci malých, pomalu rotujících planetek. Jako míru excitace rotace jsme zvolili úhlový odklon nejkratší hlavní osy planetky od vektoru momentu hybnosti. Ve světelné křivce začíná být tumbling patrný pro úhly větší než asi 15 stupňů při použití přesných fotometrických měření.

Velikost excitace se dá snadno spočítat na základě znalosti poměru orbitálního momentu hybnosti (který nese hlavně projektil) a rotačního momentu hybnosti cíle. V této práci jsme také odvodili vztah mezi tímto poměrem a úhlovým odklonem nejkratší hlavní osy planetky od vektoru momentu hybnosti.

Dále jsme srovnali specifickou energii každé srážky s mezní energií, která by už způsobila výraznou změnu struktury nebo tvaru cílové planetky. Excitace rotace bez významného poškození planetky je možná pro planetky větší než asi 100 m. V závěru diskutujeme naše výsledky a zamýšlíme se nad další prací, která by vedla k hlubšímu pochopení procesů excitace rotace planetek.

Acknowledgment

Contents

List of symbols

F	ratio of impact crater diameter to mean asteroid radius
I	inertia tensor
I_D	diagonal inertia tensor
I_1, I_2, I_3	principal inertia moments
$\omega_1, \omega_2, \omega_3$	angular velocity components
$\boldsymbol{\omega}$	angular velocity
ψ, ϕ, θ	Euler angles (in Chapter 2)
ϕ, θ	impact point coordinates
ψ	angle between $\boldsymbol{L}_{orb}$ and $\boldsymbol{L}_t$ vectors
P_{ψ}	rotation period
$P_{\bar{\phi}}$	precession period
τ	damping timescale of the excited rotation
a, b, c	target ellipsoid semiaxes
β	misalignment angle of the shortest principal axis after collision
$\boldsymbol{v_{imp}}$	impact velocity
m_t	pre collision mass of the target
m_p	pre collision mass of the projectile
$\boldsymbol{v_t}$	pre collision velocity of the target
$m^{\star}$	target post impact mass
$\boldsymbol{v^{\star}}$	target post impact velocity
$\boldsymbol{L_t}$	target pre impact rotational angular momentum vector
$\boldsymbol{L_p}$	projectile pre impact rotational angular momentum vector
$\boldsymbol{L_{orb,t}}$	target pre impact orbital angular momentum vector
$\boldsymbol{L_{orb,p}}$	projectile pre impact orbital angular momentum vector
$\boldsymbol{L^{\star}}$	target post impact rotational angular momentum vector
$\boldsymbol{L^{\star}_{orb}}$	target post impact orbital angular momentum vector

$\boldsymbol{L_{\text{ejecta}}}$	ejecta angular momentum vector
$\mathsf{I_t}$	target inertia tensor
$\mathsf{I_p}$	projectile inertia tensor
$\boldsymbol{\omega_t}$	target angular velocity
$\boldsymbol{\omega_p}$	projectile angular velocity
η	momentum transfer efficiency in normal direction
ζ	momentum transfer efficiency in tangential direction
$\boldsymbol{v_{\text{norm}}}$	normal direction impact velocity
$\boldsymbol{v_{\text{tang}}}$	tangential direction impact velocity
$\boldsymbol{E_1}, \boldsymbol{E_2}, \boldsymbol{E_3}$	inertia tensor eigenvectors
$\boldsymbol{E_3}$	eigenvector in direction of the shortest principal axis
K_1, K_2	parameters in impact event scaling laws
μ, ν	scaling exponents in impact event scaling laws
ρ	target mass density
δ	projectile mass density
$\bar{Y}$	target material strength

Preface

This PhD thesis is focused on a single topic and does not diverge into many different areas. At the beginning, there was a single question: could collisions between asteroids cause tumbling? Simple question, many problems. Although elementary physics gives the positive answer, it starts to be complicated if one goes into deeper details and investigates all the effects connected with high speed collisions described in the literature. This 'tree of complexity' is rather typical for any problem we encounter not only in physics but also in our lifes.

I worked on my PhD thesis at the Deptartment of Theoretical Physics and Astrophysics of Masaryk University in Brno, which is my alma mater and also at the Astronomical Institute of the Academy of Sciences of the Czech Republic in Ondřejov, which is a home institution of my supervisor, Petr Pravec. In Brno I spent most of the time studying literature, writing and testing my program and also teaching students the basics of astronomical observations and data reduction. In Ondřejov I usually discussed the problems I encountered during my work with Petr and we planned further work.

Although my present work concerns theory and modeling, I started my undergraduate studies with observations and during my PhD studies I had several unique opportunities to go back to my roots and observe at some excellent observatories. With my colleagues in Brno I also took part in countless starparties to observe spectacular phenomena and the sky view always reminded me where I started my journey.

During my studies in Brno I assisted my colleague Filip Hroch in teaching younger students the basics of astronomical observations at Monteboo observatory in Brno and later at Vyškov observatory. For me it was extremely useful experience since teaching someone is one of the best way to learn yourself. Only then I realized that explaining things clearly is very difficult and one has to pay attention so that people really listened to him and understood.

Tomáš Henych
autumn equinox 2013

1

Introduction

1.1 Tumblers

The very first photometric observations of asteroids showed harmonic variations of their light. This was explained as the reflection of asteroid's rotation and irregular shape or less likely the variation of albedo of its surface. All the observed lightcurves showed only regular variations which were understood as indicative of principal axis (PA) rotation state of asteroids.

Kopal (1970) published the note about the axial rotation of asteroids, exepressing the surprise, that no beat phenomena connected with free precession were observed in asteroid lightcurves. It was based on an erroneous assumption of the most important damping mechanism at work (jovi-solar attraction). The more realistic model of precession damping was given by Burns and Safronov (1973). The axis alignment is presumably caused by stress–strain cycling within the body resulting in internal energy dissipation. From energetic point of view, the precession, or an excited state of rotation, has higher energy than a basic state of rotation. Therefore internal energy dissipation in an irregular body causes the gradual decrease of the rotational energy until the basic state of principal axis rotation is reached. The

lowest energetic state of rotation is the one about the axis of maximum moment of inertia.

The timescale of this process and an average nutation angle of the asteroid's rotation caused by random collisions was also estimated by Burns and Safronov (1973). They concluded that the vast majority of then known asteroids should be in basic state of rotation, although several asteroids were mentioned as suspect of being in an excited rotation state.

Twenty years later, the problem of timescales of damping the asteroid rotation was revised by Harris (1994). The impulse to do so were the new lightcurve data escpecially of slowly rotating asteroids, which, in some cases, exhibited long sought beats, indicating the wobbling. Harris (1994) also proposed the term *tumbler* to label the bodies being in non principal axis (or NPA) rotation state. The most prominent was the case of 4179 Toutatis, a small Apollo asteroid, which made a close approach to Earth in December 1992. Both, photometric and radar data taken during the observing campaign showed that its lightcurve does not show the traditional harmonic pattern and Toutatis became the first confirmed tumbling asteroid (Spencer et al. 1995, Ostro et al. 1995).

The review on tumbling asteroids was published by Pravec et al. (2005). It presented the known and newly discovered tumblers among the asteroids, desribed their lightcurves with two dimensional Fourier series and also gave a brief overview of possible mechanisms causing the excitation of rotation. The tumbling can be expected for small asteroids with long or extremely long rotation period or for small asteroids with very short rotation period. The latter are usually observed among the NEAs, which is caused by observational bias towards closer and therefore brighter asteroids.

At present time, several tens of asteroids are known to be in NPA rotation state or are suspect of this based on photometric observations (Pravec, pers. communication, 2013, see the Fig. 2.4 in Sect. 2.4). Even though there is an increasing effort of both professional and amateur astronomers to observe those asteroids with longer rotation periods, the observation remains relatively difficult compared to that for shorter period ones in PA rotation states. The observer has to link the observations from individual nights at least in his internal photometric system, which needs some effort, a lot of experience and also very good atmospheric conditions. Therefore, only a limited number of well described tumblers are known; a number of other asteroids remain suspects for NPA rotators.

1.1.1   What causes tumbling?

Since the first consideration of tumbling asteroids, it was obvious to ask about the cause of tumbling. The natural tendency of all bodies is to remain in the lowest energetic possible state, which is the pure spin (rotation about the principal axis with the largest moment of inertia). There were several proposed processes causing the excitation of rotation which can be found in a review of Paolicchi et al. (2002). Here we give a brief overview.

Collisions are one of the most important processes for small bodies. They are responsible for their size distribution (Donnison and Sugden 1984) as well as for the rotation rates of the medium sized to large bodies with diameter $> 40\,\mathrm{km}$ (Pravec and Harris 2000). Possibly, they could also excite their rotation, which is the main topic of this work.

Other processes possibly responsible for the change of the asteroid rotation are connected with the solar radiation. Paddack (1969) described the effect of solar radiation pressure torque. Rubincam (2000) proposed a torque given by absorption of sun radiation and its re-emission as thermal radiation by irregular asteroid surface with a thermal inertia (Yarkovsky–O'Keefe–Radzievskii–Paddack, or YORP, effect).

Vokrouhlický et al. (2007) constructed an analytical model to follow the evolution of the asteroid spin throughout its life. They found that YORP can substantially slow down the rotation of the asteroid and eventually leads to onset of tumbling. They note, however, that this process is always limited by collision powerful enough to seriously change the rotation of the asteroid.

Another process affecting the rotation of planet crossing asteroids can be gravitational torque during close planetary flyby (Richardson et al. 1998, Black et al. 1999, Scheeres et al. 2000). This process cannot, however, explain the Main Belt tumblers.

Comets, which can also have excited rotation, can be excited by torque caused by mass ejection (Peale and Lissauer 1989). This process is also important for some asteroids. The ejecta related to the large subcatastrophic collision preferentially escape in the direction of rotation (Dobrovolskis and Burns 1984) and for the off-axis collision the torque could cause the excitation of rotation.

Laboratory experiments of Giblin and Farinella (1997) simulating the disruption of asteroid in the Main Belt showed that only small fraction of fragments produced in the catastrophic impact experiment were tumbling. This suggests that during the catastrophic disruptions of the asteroids, only small part of the fragents may be

tumbling from its birth. For those tumbling fragments it is necessary to take into account damping timescale to find the probability of their observable tumbling.

1.2   Large craters on asteroids

The most common asteroid surface feature are the impact craters, according to direct observations of asteroids and small planetary satellites with rocky surface. It is significant that the largest craters on the bodies visited by the space probes are huge compared to the body size. The relative size of the crater is usually described by the $F = D/R_{\mathrm{m}}$ ratio, where D is the crater diameter and R_{m} is the mean body radius – the radius of a sphere of the same volume (Thomas 1999). Large craters on such bodies have $F \sim 1$ and the largest observed even up to $F \sim 1.3$ (Burchell and Leliwa-Kopystynski 2010). There is also an indirect evidence for even larger crater on 90 Antiope (Descamps et al. 2009) which could have $F \sim 1.6$.

This fact tempts to the the following question: could large collisions that left such huge impact craters on those bodies lead to the observable excitation of their rotation? There is a tumbling asteroid that suggests a positive answer. Main Belt asteroid 253 Mathilde with the mean radius of 26.4 km is a tumbler with very slow rotation (main period 418 h, Mottola et al. 1995). It was visited by NEAR spacecraft in June 1997 and about 60% of its surface was imaged (Veverka et al. 1999). It was found that the surface is covered by several huge impact craters. The largest one has a diameter of 33 km (Veverka et al. 1997) and the size of the other large crater (five to six in total on the imaged half of the body) are also comparable to the mean radius of the whole asteroid. Mathilde was a subject to enormous bombardment and these collisions had to significantly affect its rotation.

1.3   Subcatastrophic collisions

In this work, we consider the effect of subcatastrophic collisions on the rotation of the asteroid. Previously, only Gauchez and Souchay (2006) investigated the role of small collisions on the rotation of the asteroid in cratering and also in accretion regime but they did not concentrate on the onset of tumbling. Our work is the first to address this question.

The subcatastrophic collisions are those with the specific impact energy (kinetic energy of the projectile per unit target mass) smaller than some shattering criterion. This criterion discriminates the regime of collisions that leads to a serious change of the structure and possibly the shape of the asteroid. It is described in more detail in Sect. 4.3. We are mainly interested in the excitation of rotation (i.e., the change from principal axis to non principal axis rotation), but we also deal with the change of the rate of the spin.

In general, any non-central collision will cause the excitation of rotation, but only large enough collisions could cause *observable* excitation. In this work, we model the collision in an analytical manner, calculate the transfer of the angular momentum from the projectile to the target body and than calculate its lightcurve. After that, we simulate the observation of that lightcurve and find the relation between the observability of tumbling and the input parameters of the collision.

Chapter 2 is devoted to detailed description of tumblers' rotation state, its damping in time, the properties of lightcurves of tumbling asteroids derived mainly from photometric observations and at the end of that chapter we give an account to several significant tumblers.

In Chapter 3 we present a thorough description of our subcatastrophic collision model. We discuss the maximum size of the impact craters observed on the asteroids, the shattering criterion we use, the method for numerical calculation of the inertia tensor and the measure of the principal axis deviation after the collision. Very important is the angular momentum transfer efficiency as measured in laboratory experiments. This has been recently addressed by other investigations and there is still an ongoing discussion on this problem. Another section gives scaling laws of impact cratering we use for the calculation of the crater dimensions formed by the collision. Then we describe the calculation of the lightucrve of the asteroid and in the last section we concetrate on model limitations.

Chapter 4 gives the overview of the results we have obtained in our work. We decribe the sensitivity of results to several input parameters describing the dynamical state of the precollision asteroid or the collision circumstances. Then we show that the excitation of rotation is mainly influenced by the ratio of the projectile orbital to target rotational angular momentum and also give a simple relation between the measure of the excitation and this ratio. At the end of the chapter we plot the results of our simulations in the well known graph of the specific impact energy versus asteroid diameter.

In the last two chapters we give the conclusions of the work based on the results and we discuss further work that can be done to extend our model and test the hypothesis of the collisional origin of tumbling.

2

Tumblers

In this chapter we describe tumbling asteroids more thoroughly. We will briefly describe the dynamics of rotation of tumblers and the periods of rotation and precession, that can usually be observed in their photometric lightcurves. Then we will focus on the basic analysis of their lightcurves and pitfalls of their observations. We also describe the damping mechanism that puts tumblers back to the pure spin and a timescale estimate of the mechanism. Finally, we give a short characteristics of several significant and well described tumblers.

2.1   Inertia tensor

To describe the general rotation of a rigid body, we need to know its inertia tensor I, which is a 2nd rank symmetric tensor and therefore has six indepedent components. For each body it is possible to find such a coordinate system, where the inertia tensor has only three independent components in its diagonal. These are the principal moments of inertia and they can be found as eigenvalues of the inertia tensor. We will use the following convention for designation of principal inertia moments

throughout the thesis, $I_1 \leq I_2 < I_3$. The diagonal form of the inertia tensor (and the associated coordinate system) is found by

$$\mathsf{I}_{\mathrm{D}} = \boldsymbol{Q}^{\mathrm{T}} \mathsf{I} \boldsymbol{Q}, \tag{2.1}$$

where I_{D} is the diagonal inertia tensor, $\boldsymbol{Q}$ and $\boldsymbol{Q}^{\mathrm{T}}$ are orthogonal matrix and transposed orthogonal matrix, respectively. Its rows (and columns, respectively) are the eigenvectors of I. These eigenvectors of the inertia tensor have also a physical meaning – they are the principal axes of the body. We denote the eigenvectors $\boldsymbol{E_i}$ ($i = 1, 2, 3$) and their magnitude will be unity, since we only need to consider their directions. The direction of these eigenvectors are chosen so that they form right-handed orthogonal system.

The coordinate system with the origin at the body center of mass and axes that coincide with the principal axes of the body is preferable for description of rotation, since the inertia tensor has its simple (diagonal) form as well as other expressions. We will use this coordinate system in the following description. Otherwise, we will explicitly state that we work in the inertial coordinate system with the origin in the body center of mass.

2.2   Orientation of the body in 3D – Euler angles

For description of the rotation of tumblers we will need to solve the equations of motion of a general rotation. Before that, we need to know how to desribe the orientation of the body. There are several ways to do that, but it is usually described by Euler angles ψ, ϕ, θ. These are angles between the inertial coordinate system axes and the axes of bodily coordinate system (preferentially principal axes of the body). The convention used in this work is displayed in Figure 2.1 and it follows the so called x-convention used for instance in Samarasinha and A'Hearn (1991).

2.3   Rotation state of tumblers

The rotation energy in the body principal axis coordinate system is

$$E_{\mathrm{rot}} = \frac{L_x^2}{2I_1} + \frac{L_y^2}{2I_2} + \frac{L_z^2}{2I_3}, \tag{2.2}$$
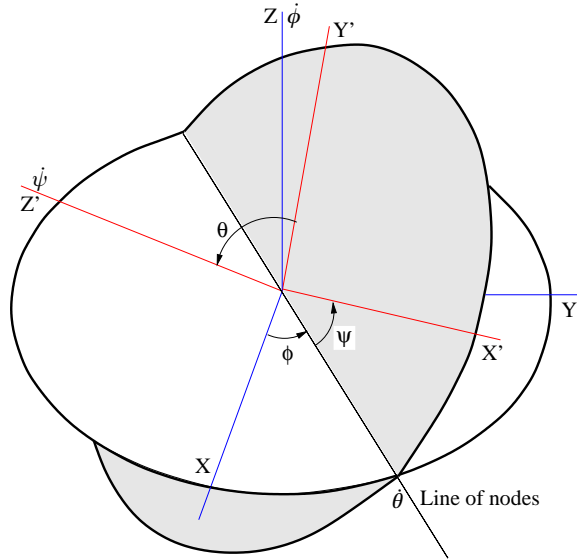
Figure 2.1   Euler angles are three angles, ψ, ϕ and θ which describe the orientation of the bodily coordinate system (shaded) with respect to the inertial coordinate system (white).

where L_i $(i = x, y, z)$ are Cartezian components of the angular momentum vector $\boldsymbol{L}$. This function has its minimum, when the body rotates about its shortest principal axis with maximum moment of inertia I_3 for a given angular momentum magnitude

$$L = L_z.\tag{2.3}$$

Most of the asteroids with observed lightcurves are in this basic state of rotation (i.e., pure spin) about the axis of maximum moment of inertia. Moreover, the rotation about that axis is a stable rotation state. The angular velocity vector $\boldsymbol{\omega}$ is aligned with the angular momentum vector $\boldsymbol{L}$ and its mutual orientation does not change in time.

There are processes that can excite the rotation of asteroids. We described them in Chapter 1 and a review of those processes can be found in Paolicchi et al. (2002) and Pravec et al. (2005). Then, the rotation state is not basic, the asteroid precesses. If there are no external torques acting on the body, we call this rotation state a free

precession. It's dynamics can be described by the Euler equations

$$
\begin{aligned}
(I_1 - I_2)\omega_1\omega_2 - I_3\dot{\omega}_3 &= 0, \\
(I_3 - I_1)\omega_3\omega_1 - I_2\dot{\omega}_2 &= 0, \\
(I_2 - I_3)\omega_2\omega_3 - I_1\dot{\omega}_1 &= 0.
\end{aligned}
\tag{2.4}
$$

where $\omega_i\,(i = 1,2,3)$ are components of the angular velocity vector. The general solution of these equations is given by kinematic Euler equations, which give the $\boldsymbol{\omega}$ components as a function of Euler angles which in turn are functions of time

$$
\begin{aligned}
\omega_1 &= \dot{\theta}\cos\psi + \dot{\phi}\sin\psi\sin\theta, \\
\omega_2 &= -\dot{\theta}\sin\psi + \dot{\phi}\cos\psi\sin\theta, \\
\omega_3 &= \dot{\psi} + \dot{\phi}\cos\theta.
\end{aligned}
\tag{2.5}
$$

It is only possible to find the explicit solution of these equations in some special cases.

2.3.1   Stability of the rotation

In this section, we will discuss the stability of rotations around principal axes because only then we can understand the processes after large subcatastrophic collision. We will follow the description of lucid physics lectures of Varnes (2004).

Let us suppose the body rotates purely about its *longest* principal axis (with smallest moment of inertia), so the angular velocity vector is

$$
\boldsymbol{\omega} = \omega_1\boldsymbol{E}_1.
\tag{2.6}
$$

When we bump the body slightly, the angular velocity vector changes to

$$
\boldsymbol{\omega} = \omega_1\boldsymbol{E}_1 + \lambda\boldsymbol{E}_2 + \mu\boldsymbol{E}_3,
\tag{2.7}
$$

where λ and μ are small disturbances. Now, we put this vector to the Euler equations 2.4 and we get

$$
(I_1 - I_2)\lambda\omega_1 - I_3\dot{\mu} = 0,
\tag{2.8}
$$

$$
(I_3 - I_1)\mu\omega_1 - I_2\dot{\lambda} = 0,
\tag{2.9}
$$

$$
(I_2 - I_3)\lambda\mu - I_1\dot{\omega}_1 = 0.
\tag{2.10}
$$

We only consider terms in λ and μ to first order, so when we neglect the first term in Eqn. 2.10, we see, that ω_1 will not change in time. We solve the other two equations by taking the time derivative of 2.8 and putting it to the 2.9 to get

$$\ddot{\lambda} = \left(\frac{I_3 - I_1}{I_2} \omega_1 \right) \left(\frac{I_1 - I_2}{I_3} \omega_1 \right) \lambda \equiv -\Omega^2 \lambda, \tag{2.11}$$

where we designated the constant in front of λ as $-\Omega^2$. Note that we would get similar equation for μ. It has a general solution

$$\lambda = A e^{i\Omega t} + B e^{-i\Omega t}, \tag{2.12}$$

where A and B are constants. There are two possible solutions, which are qualitatively different. If Ω is real, then we get oscillatory motion of λ (and μ). It means that the rotation is *stable*. If, on the other hand, Ω is imaginary, the second term of Eqn. 2.12 grows exponentialy with time and the rotation is *unstable*.

When we know this, we can analyse the Eqn. 2.11 and see, under which conditions is has stable or unstable solution. This will tell us a lot about the behaviour of rotating bodies.

If I_1 is the *smallest* moment of inertia, then

$$I_1 - I_3 < 0 \wedge I_1 - I_2 < 0, \tag{2.13}$$

their product is positive and Ω is real, we get a *stable* rotation about the shortest principal axis.

If, on the contrary, I_1 is the *largest* moment of inertia, then

$$I_1 - I_3 > 0 \wedge I_1 - I_2 > 0, \tag{2.14}$$

their product is again positive, Ω is real and we get a *stable* rotation about the longest principal axis.

If I_1 is the *intermediate* moment of inertia, then

$$I_1 - I_3 < 0 \wedge I_1 - I_2 > 0, \tag{2.15}$$

their product is negative, Ω is imaginary and we get an *unstable* rotation about the intermediate principal axis.

This is why the body will not rotate about the intermediate axis for a long time and it will tend to the stable rotation. The two stable rotation states differ by the

amount of rotational energy – rotation about the axis with *smallest* moment of in-
ertia has the *largest* energy, while the rotation about the axis with *largest* moment
of inertia has the *lowest* energy. This is presumably the rotation state of majority of
asteroids.

2.3.2   Rotation and precession periods

From the analysis of the precession dynamics, we can derive the expression for the
rotation and precession periods. The period of rotation (in ψ) is

$$P_\psi = 4K\sqrt{\frac{I_1 I_2 I_3}{(I_3 - I_2)(L^2 - 2EI_1)}},$$
(2.16)

where E is the energy of rotation and K is a complete elliptic integral of the first
kind given by

$$K = \int_0^{\frac{\pi}{2}} \frac{\mathrm{d}u}{\sqrt{1 - k^2 \sin^2 u}}.$$
(2.17)

The k^2 is a dynamical constant for a body in a specific rotation state

$$k^2 = \frac{(I_2 - I_1)(2EI_3 - L^2)}{(I_3 - I_2)(L^2 - 2EI_1)}.$$
(2.18)

This period holds for angles ψ and θ, but not for ϕ. For that angle, the expression
for period is rather complicated. It consists of two terms, one has the same period
P_ψ and the other has different period P' which is incommensurable with P_ψ. This is
why the precessing body does not at any time return to its original position (Landau
and Lifshitz 1976).

   The motion in ϕ is aperiodic in general case (unless the body has two axis equal
in length) and what is commonly used in practice is a time-averaged period $P_{\bar\phi}$ cal-
culated as (Samarasinha and A'Hearn 1991)

$$P_{\bar\phi} = \frac{2\pi}{\dot{\bar{\phi}}},$$
(2.19)

where

$$\dot{\bar{\phi}} = \frac{2}{P_\psi} \int_0^{\frac{P_\psi}{2}} \dot{\phi}\, \mathrm{d}t.$$
(2.20)

Similar expressions can be found in Kaasalainen (2001), who describes very comprehensively the nature of tumblers' lightcurves and also specifics of the inversion method for those lightcurves.

There is a useful constraint on the ratio of rotation to precession period derived in Samarasinha and A'Hearn (1991)

$$\frac{P_\psi}{P_{\bar{\phi}}} \geq \sqrt{\frac{I_2 I_3}{(I_2 - I_1)(I_3 - I_1)} - 1}\,, \qquad (2.21)$$

which holds for the so called Long axis modes (LAMs), when $L^2 < 2EI_2$ and

$$\frac{P_\psi}{P_{\bar{\phi}}} \geq \sqrt{\frac{I_1 I_2}{(I_3 - I_2)(I_3 - I_1)}}\,, \qquad (2.22)$$

which is valid for the Short axis modes (SAMs), when $L^2 > 2EI_2$. From this it can be derived that for SAMs holds

$$\frac{P_\psi}{P_{\bar{\phi}}} > 1\,. \qquad (2.23)$$

2.3.3   Damping of the excited rotation

There are several processes that can excite the rotation of asteroids, yet we observe most of them in principal axis rotation state or close to it. It is caused by nature of the excited rotation itself.

When we observe the rotation of the body in the bodily reference frame, the angular velocity vector is travelling through the body on the surface of a cone which is axialy symmetric about the fixed angular momentum vector. The body is then rotating about the instantaneous angular velocity vector. Let us consider a small volume of the asteroid material. As the body tumbles, this volume will experience variable centrifugal acceleration, because the actual axis of rotation is constantly changing. This means that the asteroid experiences time variable stress and strain, depending on the position in the body caused by variable centrifugal acceleration. This acceleration is symmetric about the rotation axis which is, however, changing its direction.

This stress–strain cycling leads to the energy dissipation which causes the constant damping of the excited rotation, finally leading to the principal axis rotation, as it is the rotation state with the lowest energy (see Section 2.3).

A particular importance has the estimate of the timescale of the excitation rotation damping. It has been done by several authors for various situations in planetary astronomy, but specifically for the case of asteroids this was published by Burns and Safronov (1973). They estimated the timescale τ as

$$\tau = \frac{\mu Q}{\rho K_3^2 r^2 \omega^3}, \tag{2.24}$$

where μ is an asteroid rigidity, Q is a quality factor of its material and ρ its density, r its radius and $\omega = 2\pi/P$ is the angular speed (P being the period of rotation). K_3^2 is a shape factor whose value depends on the asteroid oblatness. The quality factor describes the energy loss per stress–strain cycle

$$\Delta E = \frac{2\pi E}{Q}, \tag{2.25}$$

E is the part of the total strain energy of the body which oscillates during the wobble motion.

Burns and Safronov (1973) calculated this timescale for several asteroids of various sizes and shapes for which the rotation period was known. They concluded that for a reasonable choice of the physical parameters in Eqn. 2.24, the timescale is much shorter than the age of the Solar System and so the rotation axis of the asteroid is aligned with the angular momentum axis shortly after the excitation event (e.g., a collision). That is why we usually observe the single periodic lightcurve for majority of asteroids.

They pointed out, however, several asteroids for which the alignment would take much longer time. These would be small and slowly rotating asteroids presumably with irregular figure, which could be easier to observe as precessing.

The problem of damping timescales was reexamined by Harris (1994) as there were new observations of slowly rotating asteroids, for which the timescale would be longer than the age of the Solar System. Amongst them, 4179 Toutatis exhibited a very long rotation period of several days and moreover a very complex lightcurve shape. This asteroid became the first confirmed tumbler by radar (Ostro et al. 1995) and photomertric observations (Spencer et al. 1995).

Harris (1994) used the expression of Burns and Safronov (1973) and his own estimate of the asteroid material properties to give the relation between rotation

period P in hours, its diameter D in kilometers and the damping timescale τ in billions of years as

$$P \approx 17 D^{2/3} \tau^{1/3}, \tag{2.26}$$

with an uncertainty about a factor of 2.5 in the constant (given the uncertainties in the asteroid physical properties used).

The previous approaches to the damping timescale estimates were sharply criticized by Efroimsky and Lazarian (2000) and Efroimsky (2001). The latter paper contains a thorough description of the precession motion and the dissipation process itself and raises several important drawbacks of the present theory.

In their critics of the previous approaches, they stated that substantial features of physical processes during energy dissipation were overlooked or inappropriately neglected, which led to several order of magnitude underestimation of the effectiveness of the dissipation process. Moreover, they stated that the physical parameters chosen by previous authors were inadequate. They give a much shorter damping timescale, but the general form is the same as in Eqn. 2.24.

While Efroimsky (2001) calculated the stresses for a cuboid-shaped body, Molina et al. (2003) and Sharma et al. (2005) used the symmetric ellipsoid of rotation for their calculations. Sharma et al. (2005) presents his complete solution of damping for oblate and prolate spheroids but also gives the overview of the previous papers on the topic including that of Efroimsky and Lazarian (2000), Efroimsky (2001) and Molina et al. (2003). They concluded that all the previous authors agree on the functional form of the damping timescale

$$\tau = D' \frac{\mu Q}{\rho r^2 \omega^3}, \tag{2.27}$$

but differ through the constant D' (all the quantities have the same meaning as in 2.24 above). In Sharma et al. (2005), D' is a constant of the order of few hundreds and it is a function of the shape of the body $D'(h)$ given by the aspect ratio h of the length of the shortest axis to the longest axis.

The damping time in the form of Harris (1994) with the same choice of μ and Q and with $D' = 200$ which roughly corresponds to oblate or prolate bodies with a/c either 2 or 1/2 is

$$\tau = 0.24 \cdot 10^{-3} \frac{P^3}{r^2} \quad \text{or} \quad P \approx 10 D^{2/3} \tau^{1/3}, \tag{2.28}$$

when using the same notation and units as Harris (1994) – billions of years for τ, period of rotation P in hours and diameter D in kilometers. Both expressions, 2.28 and 2.26, are in good agreement.

2.4   Lightcurves of tumblers

In most cases, the rotational state of tumblers is deduced from their photometric lightcurves. Asteroids found in the principal state of rotation exhibit single periodic lightcurves while tumblers have more complicated two periodic lightcurves.

There is, however, another group of asteroids that have usually two periods in their lightcurves – binary asteroids. In this case, the most common situation is that the main period present in the lightcurve reflects the rotation of the primary body (the larger one), it is slightly modulated by the rotation of the secondary (sometimes not detected) and for a favorable viewing geometry, there are dips in the lightcurve caused by mutual eclipses and occultations of the bodies (Pravec and Hahn 1997).

The nature of tumblers' lightcurves is different. It reflects their complex state of rotation which is two periodic. One period, P_ψ, is the rotation period about the extremal axis, and $P_{\bar\phi}$ is the precession about the angular momentum vector $\boldsymbol{L}$. The third period connected with the third Euler angle, θ, is equal to the rotation period (Landau and Lifshitz 1976).

Photometric observations of tumbling asteroids are generally more demanding than observations of singly-periodic asteroids. The rotation period of an asteroid in principal axis rotation is typically a couple of hours and so it is possible to observe the whole rotation in one night (depending on the length of the night).

Tumblers, on the other hand, prevail amongst the bodies with long rotation periods (on the order of tens to hundreds hours) amongst larger asteroids or with extremely short periods amongst very small asteroids. Both of these extreme lightcurves are rather difficult to observe.

Long period lightcurves do not have to be sampled so frequently as the lightcurves of the common asteroids and so these tumblers can be observed as complementary targets to other asteroids. Usually only a small part of the lightcurve is observed during one night and so it is critical to link it to the observations from other nights to cover the complete phasecurve. It is even more beneficial to calibrate the observations in the standard photometric system. Then, it can be combined with
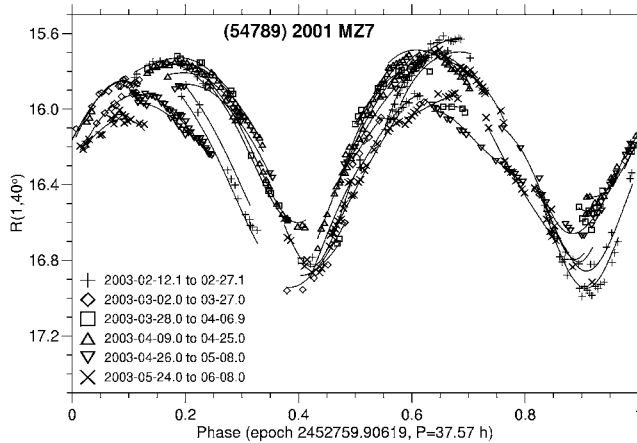
Figure 2.2   A long periodic lightcurve of tumbler (54789) 2001 MZ7 phased with one of the periods of 37.57 h. Together with datapoints, pieces of the best fit full two dimensional 4th order Fourier series with the periods of 37.57 h and 52.79 h are plotted as well. Vertical axis is R magnitude for a specific solar phase angle. Credit: Pravec et al. (2005).

observations by other observers from different observing sites (different longitudes) and the long period lightcurve can be obtained more effectively. It is necessary to cover the lightcurve of long period tumblers a few times so that the tumbling is definitely confirmed (see Fig. 2.2).

The observational strategy needs to be adapted also for the short period lightcurves. The exposure time should be optimized in order not to smear details of the lightcurve whose period can be on the order of several minutes (see Fig. 2.3). Then, for small and faint asteroids, we need to use a large enough telescope so that we can keep the exposure time at its optimum (Pravec et al. 2000; the case of 2000 WL107 in Pravec et al. 2005).

To analyze the lightcurves of tumblers, Kaasalainen (2001) suggested a two dimensional Fourier series technique. It is now commonly used for the analysis of tumblers lightcurves and it was also used in the review of Pravec et al. (2005). We
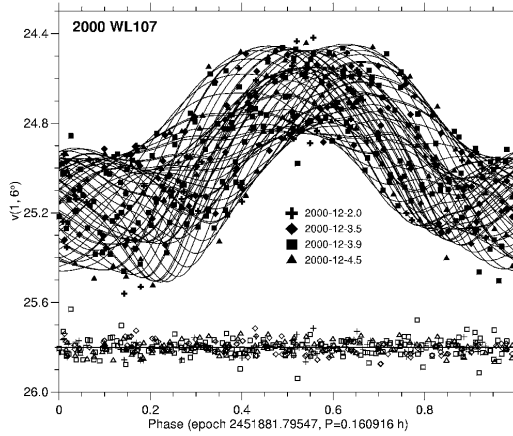
Figure 2.3   A short periodic lightcurve of asteroid 2000 WL107 folded with the period of
0.160916 h. The best fit full two dimensional 4th order Fourier series with the
periods of 0.160916 h and 0.218834 h and residuals of the fitted points are plot-
ted as well. Vertical axis is V magnitude for a specific solar phase angle. Credit:
Pravec et al. (2005).

reproduce it here in the convenient form

$$F\left(\psi(t),\phi(t)\right)\doteq F^{m}(t)=C_{0}+\sum_{j=1}^{m}\left[C_{j0}\cos\frac{2\pi j}{P_{\psi}}t+S_{j0}\sin\frac{2\pi j}{P_{\psi}}t\right]+$$
$$+\sum_{k=1}^{m}\sum_{j=-m}^{m}\left[C_{jk}\cos\left(\frac{2\pi j}{P_{\psi}}+\frac{2\pi k}{P_{\bar{\phi}}}\right)t+\right.$$
$$\left.+S_{jk}\sin\left(\frac{2\pi j}{P_{\psi}}+\frac{2\pi k}{P_{\bar{\phi}}}\right)t\right],\qquad(2.29)$$

where C_0 is the mean reduced light flux, C_{jk} and S_{jk} are the Fourier coefficients
of the series, P_ψ and $P_{\bar{\phi}}$ are the period of rotation and mean period of precession,
respectively, t is the time. In practice, it is difficult to assign the found periods to ro-
tation and precession, although we could make a learned guess using the Eqn. 2.23
provided we have additional information about the shape of the body, e.g., from
radar data.

The graph of spin rate (or rotational period) vs. asteroid diameter is a very use-
ful tool for investigation of properties of asteroids. It is displayed in Fig. 2.4 with

highlighted tumblers and well studied PA rotators among slow rotating asteroids. Tumblers seem to prevail below the 0.45 b.y. line which is a much longer time than the typical dynamical lifetime of the Near Earth Asteroids (NEAs), but it is shorter than the lifetime of the Main Belt asteroids. There are exceptions to this rule and also many slow rotators have not their rotation periods well established. Therefore, this subject still needs a lot of investigation, collecting photometric data and developing theory and numerical modeling.

2.5   Significant tumblers

Currently, we know a couple tens of tumblers or asteroids that are seriously suspicious of tumbling. The data allow some preliminary statistical treatment, but first we want to describe some of the known tumblers and to discern between principal axis (PA) rotators and non principal axis (NPA) rotators in disputable cases. As this is not the main objective of this thesis, we will only point out some typical and interesting tumblers.

2.5.1   4179 Toutatis

The first known tumbler is 4179 Toutatis. It is a small Apollo asteroid discovered in January 1989 by C. Pollas in Caussols, France (Yeomans 2013b, Marsden 1989) and designated as 1989 AC. Later precovery observations were found and the asteroid was identified with 1934 CT. It is named after the Celtic god who was a tribal protector in ancient Gaul and Britain. His name is well known to every fan of the Asterix comics.

Toutatis is a Near Earth Asteroid and it makes very close approaches to Earth. This was due to happen in December 1992, when Toutatis passed by Earth at minimum distance of 3.6 million kilometers or less than 10 lunar distances (mean distance of the Moon from the Earth). This close approach was well employed for the detailed study of Toutatis characteristics. Spencer et al. (1995) presented the unusual lightcurve of Toutatis which was explained by its NPA rotation. This was supported by radar observations of Ostro et al. (1995) who also presented extremely irregular shape of Toutatis with heavily cratered surface. More on the NPA rotation based on radar observations was given by Hudson and Ostro (1995). Moreover, the
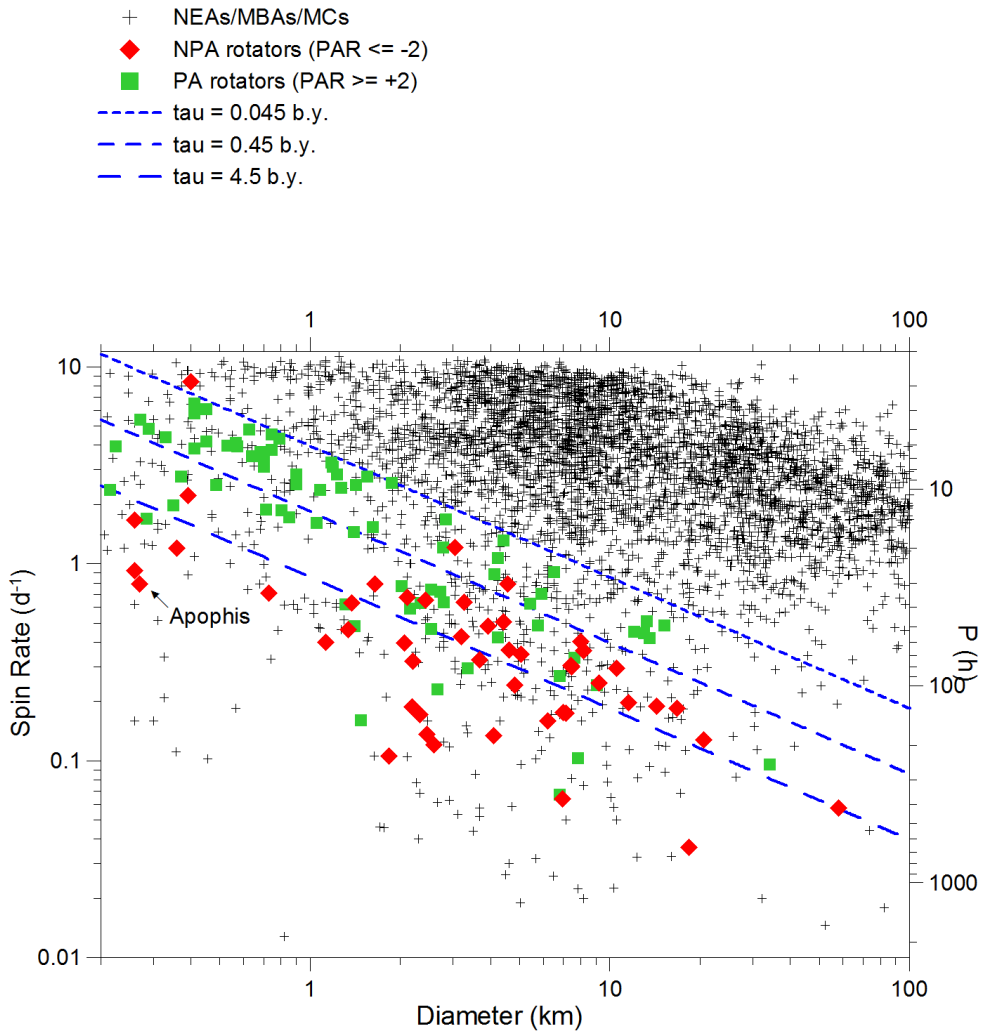
Figure 2.4 The graph of spin rate (and period of rotation) as a function of the asteroid diameter with highlighted slow tumblers (red diamonds) and slow PA rotators (green squares). The blue straight lines indicate the damping timescale of the excited rotation in billion years (see Sect. 2.3.3 for details). For the definition of the PAR codes see Pravec et al. (2005). NEAs are Near Earth Asteroids, MBAs are Main Belt Asteroids and MCs are Mars Crossers. Note that a part of the graph which contains small fast asteroids including a few tumblers is outside the plotted range. Credit: Pravec et al. 2013, pers. communication – CD8 workshop talk.

3D model was created and dimensions along the principal axes of the figure were estimated as 1.92, 2.40 and 4.60 km with an uncertainty of 0.1 km.

There were also other observations. Noll et al. (1995) used the planetary camera of the Hubble Space Telescope to directly image Toutatis. Their size estimate was in good agreement with other measurements.

The 1996 apparition of Toutatis brought new opportunity to refine the results of previous measurements. Ostro et al. (1999) gives more accurate surface properties, rotational state and also presents a shape model. Moreover, the radar observations substantially improved the asteroid's orbit in the Solar System. Kryszczyńska et al. (1999) analyzed the lightcurve of Toutatis and compared it with a synthetic lightcurve of freely precessing body. They concluded it was in good agreement and pointed out possible causes of apparent discrepancies between the periods of rotation and precession derived from photometric and radar observations.

The photometric data were later reanalyzed by Mueller et al. (2002) and previous results were confirmed independently. They obtained mean long axis precession period $P_{\bar{\phi}}$ of 7.38 days and rotation period around the long axis P_{ψ} of 5.38 days. Hudson et al. (2003) presented high resolution model of Toutatis based on 1992 and 1996 radar data which shows fine topographic details down to the resolution limit of $(34\,\mathrm{m})^2$. The model is shown in Fig. 2.5.

On 13 December 2012 Chinese probe Chang'E 2 made a flyby of Toutatis and took some very high resolution images. The closest flyby distance was only 3.2 km and the resolution about 10 m/px. One of those high resolution images is in Fig. 2.6. At the same time, radar observations were made using the 70 m Deep Space Network antenna at Goldstone, California (Benner 2012). Preliminary comparison of direct images made by Chang'E 2 and the radar model shows a very good correspondence.

As Toutatis makes its close approaches to Earth every four years, it will be certainly the target of the further research and is already the best examined tumbler.

2.5.2   253 Mathilde

Mathilde is the largest known tumbler with the mean radius of 26.5 km (Thomas et al. 1999). It was discovered by Johann Palisa in Vienna, Austria, in 1885 (Yeomans 2013c) and it was named after the wife of astronomer Moritz Loewy, the vice director of the Paris Observatory.
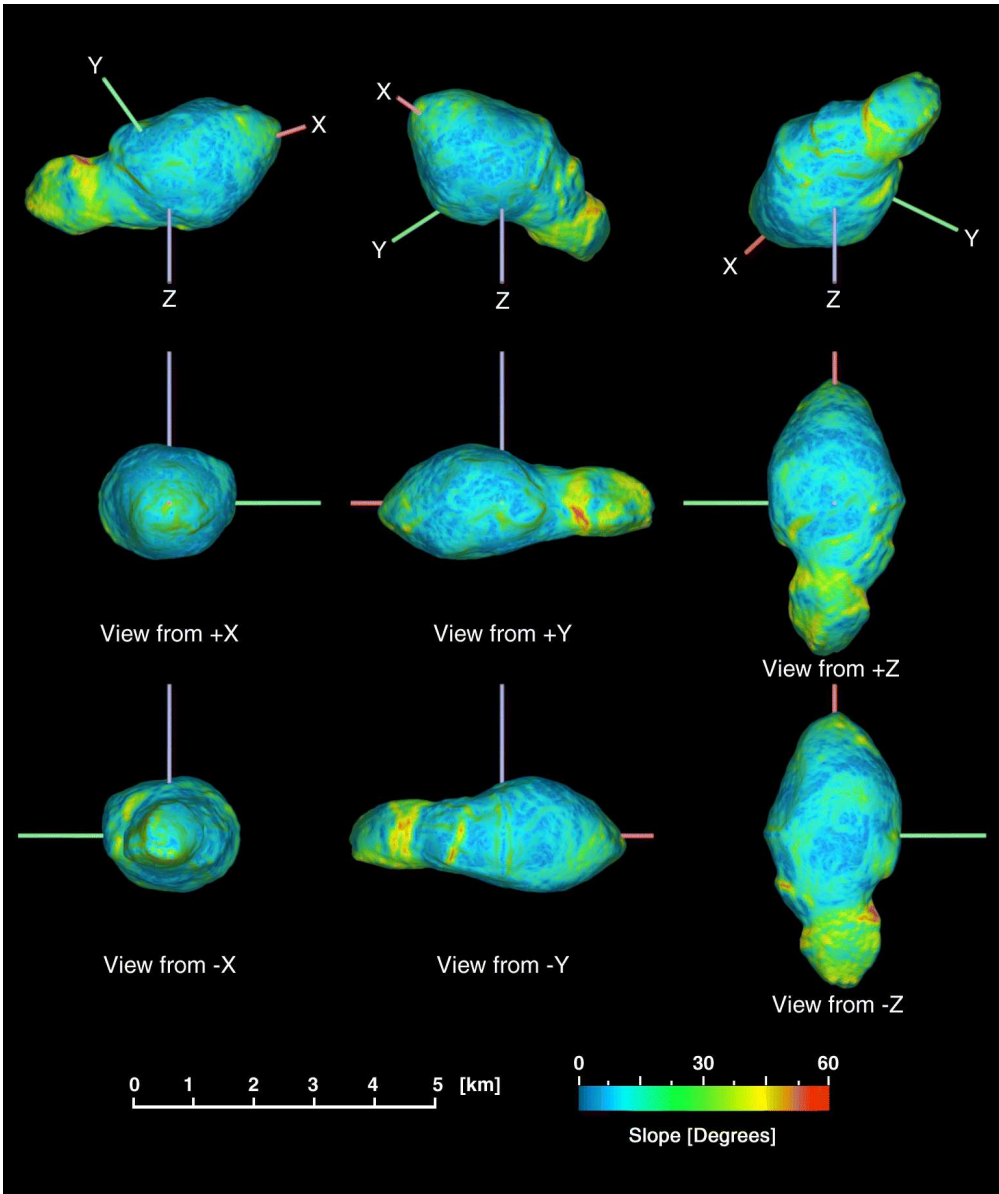
Figure 2.5 The high resolution model of 4179 Toutatis based on radar observations of Hudson et al. (2003) and Hudson and Ostro (1995) made with Goldstone and Arecibo radiotelescopes. The areal resolution of $(34\,m)^2$ is comparable to Galileo probe highest resolution images of Dactyl (the moon of 243 Ida) or NEAR Shoemaker's first images of Eros after orbit insertion (Hudson et al. 2003).
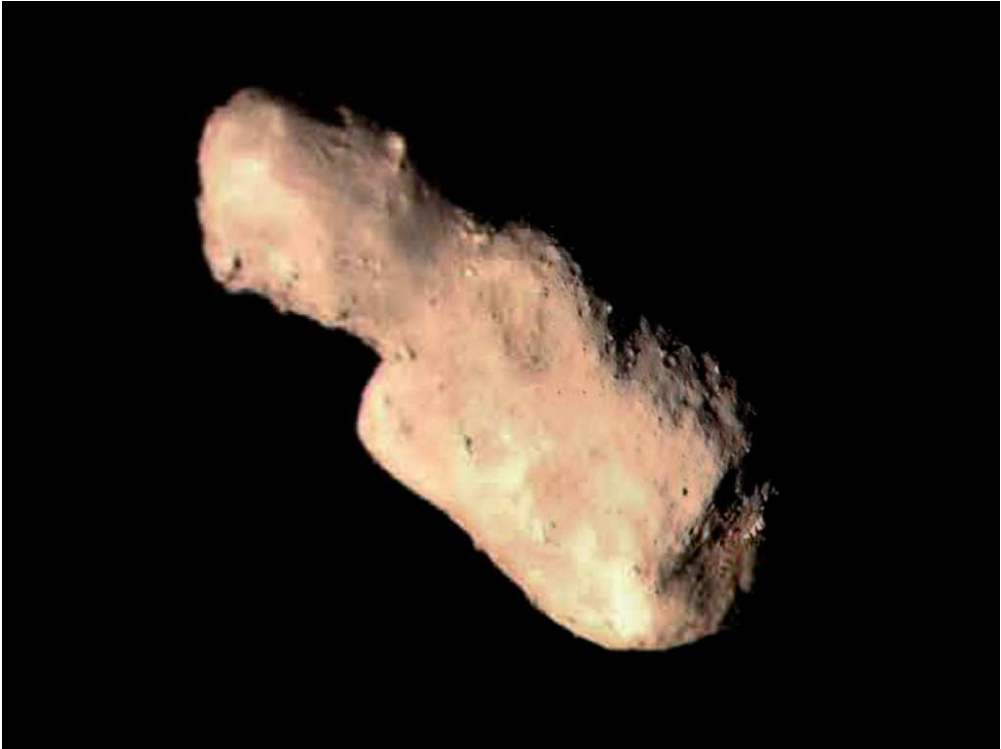
Figure 2.6   High resolution image of 4179 Toutatis taken by Chang'E 2 space probe during its close flyby. The image was taken from the distance of 93 km and the resolution is about 10 m/px. Very fine structures including many small impact craters are visible. Credit: Chinese Academy of Sciences/Daniel Macháček (Macháček 2012).

It caught attention when it became the flyby target of the NASA's Near Earth Asteroid Rendezvous (NEAR) Shoemaker mission (Dunham and McFadden 1994). It was decided that the probe will observe Mathilde and so thorough observations were requested before the flyby date. Mottola et al. (1995) made photometric observations and obtained very unusual result indicating extremely slow rotation – the main period is 418 h. During the flyby of the NEAR Shoemaker, many observations were made. Yeomans et al. (1997) measured the mass of Mathilde of $(1.033 \pm 0.044) \cdot 10^{20}$ g from tracking data of the NEAR Shoemaker. Together with the measured dimensions of the body (and its volume), this gives a very low bulk density of 1.3 ± 0.2 g cm^{-3}. If we assume the density of the material forming Mathilde as 2.8 g cm^{-3}, then we get the porosity higher than 50%.

Veverka et al. (1997) presented images of Mathilde taken by NEAR Shoemaker during its close flyby on 27 June 1997. The finest resolution of the images was about 160 m/px at closest approach (1212 km). They showed very dark surface of this C type asteroid with estimated albedo of 0.035–0.050. The most prominent features were huge craters, perhaps relics of tremendous collisions. The largest crater, later named Karoo, has the diameter of 33 km and it is probably the youngest of all imaged impact craters on Mathilde. The images showed, however, at least four other large craters with diameters exceeding 20 km (see Fig. 2.7).

This provoked the question on how could Mathilde survive such heavy bombardment without being completely dispersed. Moreover, there should be large amount of ejecta in the older craters from the more recent ones, but this was not observed. The answer was proposed by Housen et al. (1999), who investigated the compaction mechanism of crater formation indstead of excavation process. They carried out laboratory experiments and proved that not only can be craters packed very near to each other without disturbing the older one but also this mechanism can explain the observed lack of ejecta.

We presented here only brief overview of measurement results of the NEAR Shoemaker mission's flyby of Mathilde. Very thorough and detailed description of those results and surprising facts can be found in the first quarter of Icarus 140 Volume, Issue 1 (Elsevier, Philadelphia, USA). The overview of the NEAR Shoemaker mission flyby of Mathilde is given by Veverka et al. (1999).

Figure 2.7   Overall image of 253 Mathilde as taken by NEAR Shoemaker spacecraft flyby of this large tumbler on its route to 433 Eros. The largest impact crater is Karoo, there is a crater Kuznetsk on the 'northern' surface and crater Damodar on the 'southern' surface. Credit: Veverka et al. (1999).
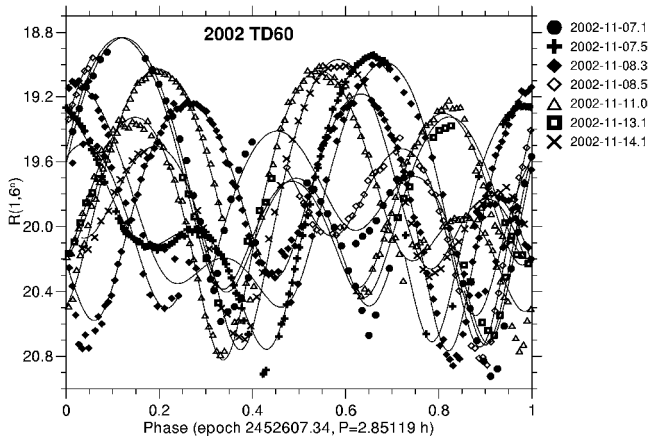
Figure 2.8   Lightcurve of 2002 TD60 folded with the period of 2.85119 h (various symbols)
and the best fit full two dimensional 3rd order Fourier series with the periods
of 2.85119 h and 6.7841 h (lines). Vertical axis is R magnitude for a specific solar
phase angle. Credit: Pravec et al. (2005).

2.5.3   2002 TD60

This small Amor asteroid has been thoroughly observed in its apparition in late
2002. Both photometric observations from various observatories (Pravec et al. 2005)
and radar observations from Arecibo were made (Benner et al. 2008). The rota-
tional state was well described by photometric observations, the two periods were
$P_1 = 2.8513 \pm 0.0001$ h and $P_2 = 6.783 \pm 0.002$ h. From those observations it is not
possible to discern the period of rotation and precession, respectively. The sample
lightcurve of TD60 can be found in Fig. 2.8.

The photometric data also allowed the modeling of the asteroid to find the di-
mensions of the triaxial ellipsoid representing the body and orientation of the an-
gular momentum vector. The dimensions of the asteroid were estimated from both
type of observations (photometric and radar) as $(310 \times 200 \times 110)$ m. Other results
can be found in Pravec et al. (2005).

2.5.4   99942 Apophis

This small ($D = 0.46 \pm 0.08$ km) SQ type (Pravec et al. 2013, pers. communication – CD8 workshop talk) Near Earth Asteroid is nowadays under a very close inspection by many observers and theoreticians. It is caused by the predicted very close flyby of the asteroid in between the Earth and Moon in April 2029 and even more by its very close flybys in 2036 and 2068 with a non-zero probability of the collision with the Earth (Farnocchia et al. 2013).

It was discovered at Kitt Peak National Observatory in Arizona, USA in 2004 (Yeomans 2013d). The name is derived from Ancient Egyptian evil god Apep who was an enemy of Ra, the sun god. Soon it was recognized as an interesting object due to its close approaches to the Earth in the near future. It was thoroughly observed by optical telescopes as well as radars. The 2029 flyby is now very accurately determined, but there are still large uncertainties of the future flyby orbits. It is mainly caused by the Yarkovsky effect. Because of the unknown direction of the Apophis' axis of rotation we do not know the magnitude of this effect and whether the semimajor axis of its orbit is increasing or decreasing (Chesley 2006).

The situation is further complicated by the discovery of Apophis' tumbling. Although the rotation state has not been very well established yet, the preliminary results show that there are two dominant frequencies in its lightcurve, $f_1 = 1/30.56$ h and $f_2 = 1/29.04$ h with uncertainties of < 0.1 h (see Fig 2.9). Other possible solution is $f_1 = 1/30.56$ h and $f_2 = 1/34.4$ h, which is a working hypothesis to be tested by the modeling of the lightcurves (Pravec et al. 2013, pers. communication – CD8 workshop talk).

2.5.5   2008 TC3

This is so far the only known asteroid that can be classified as an extinct tumbler and also an extinct asteroid – it impacted Earth and burned some 37 km above its surface. It was discovered on 6 October 2008 by the automated Catalina Sky Survey telescope at Mount Lemmon, Arizona, USA and 20 hours later it entered the Earth atmosphere above Sudan (Jenniskens et al. 2009). The 6–7 m (Scheirich et al. 2010) asteroid exploded in the atmosphere and fragments of total mass of less than 4 kg were later recovered in the Nubian Desert in northern Sudan. These are now known as Almahata Sitta meteorites named after the train station number 6 (the translation of that name).
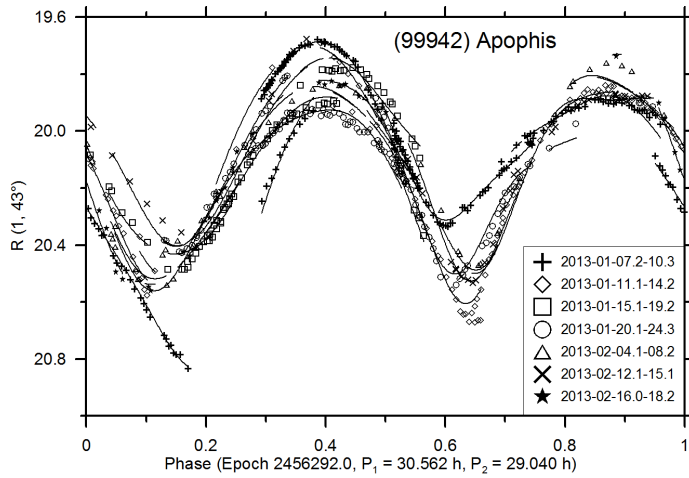
Figure 2.9   Lightcurve of 99942 Apophis in 2013 and the best fit two dimensional Fourier series with the periods of 30.56 h and 29.04 h. Credit: Pravec et al. 2013, pers. communication – CD8 workshop talk.

The lightcurves of 2008 TC3 taken in the short time between its discovery and the disappearance in the shadow of the Earth showed that it was a fast tumbling asteroid in LAM (long axis mode). The modeling of Scheirich et al. (2010) gave two almost mirror solutions with periods $P_\psi = (99.19 \pm 0.03)\,\text{s}$ and $P_\phi = (96.99 \pm 0.05)\,\text{s}$ for the first solution and $P_\psi = (99.20 \pm 0.04)\,\text{s}$ and $P_\phi = (97.02 \pm 0.05)\,\text{s}$ for the second solution. The results also included angular momentum vector orientation, principal moments of inertia and the shape model (see Fig. 2.10). Part of the lightcurve used for the modeling is displayed in Fig. 2.11.
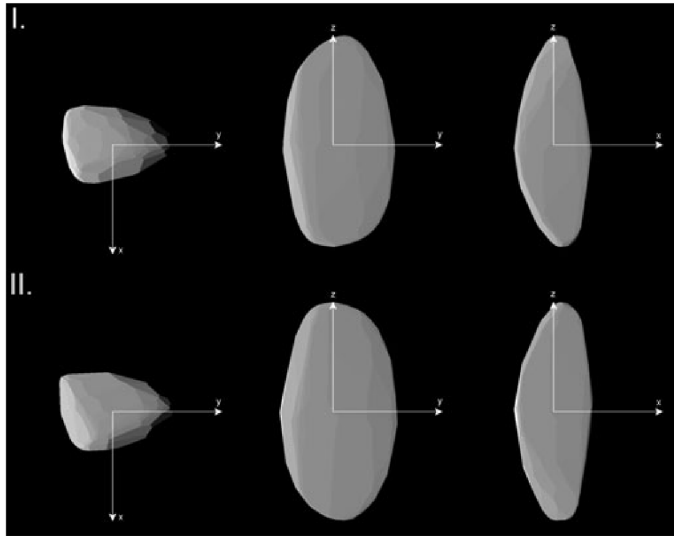
Figure 2.10   The 3D model of the 2008 TC3 made by lightcurve inversion method. Two
               mirror solutions are displayed in three viewing geometries. Credit: Scheirich
               et al. (2010).
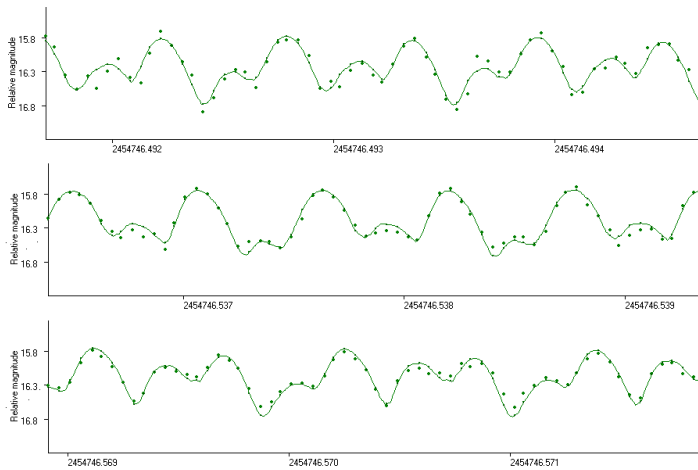
Figure 2.11   Lightcurve of 2008 TC3 on 6–7 October 2010 and the best fit two dimensional
               4th order Fourier series with the periods of 49.0338 s and 96.987 s. Horizontal
               axis is Julian day, vertical axis is relative magnitude. Credit: Pravec et al. 2013,
               pers. communication – CD8 workshop talk, Scheirich et al. (2010), data taken
               by M. Kozubal and R. Dantowitz.

3

Subcatastrophic collision model

This chapter is devoted to a thorough description of our subcatastrophic collision model. We will describe the cratering mechanism and scaling laws used for the calculation of the impact crater dimensions, angular momentum conservation and efficiency of its transfer to the impacted asteroid, the calculation of the post impact body lightcurve and the detection of tumbling and also the shattering criterion of the asteroids. We will argue on why we think our model is realistic and we will discuss its drawbacks and possible improvements as well.

3.1   Brief description of the model

We constructed the analytical model of subcatastrophic collision between two bodies to explore its effect on the rotation of the asteroid. We mainly focused on the possibility to excite its rotation by such collision, although other dynamical characteristics are calculated as well. We only consider cratering events in our model as we think it is the most probable process of small hypervelocity collision. Larger collisions that have more complex scenario are not included in our simple model.

Here we give description of our model in a nutshell for lucidity and discuss its features in detail in the following separate sections. At the beginning, there are two bodies described by a set of physical, dynamical and shape parameters (size, mass density, velocity etc.) that experience hypervelocity collision – the target and the projectile.

The projectile is completely destroyed and an impact crater is created on the surface of the target. The dimensions of the impact crater are calculated by using the scaling laws which extrapolate the outcomes of the laboratory impact experiments to asteroid dimensions. They are based on point source approximation of the impact (Holsapple 1993; Holsapple and Housen 2007).

Then we use momentum and angular momentum conservation laws to calculate the angular momentum transfered to the target. We consider some efficiency of that transfer obtained in laboratory experiments. Other possibilities are discussed later in Section 3.2.8.

After that we recalculate the dynamical characteristics of the target (mainly its inertia tensor), calculate its rotational lightcurve and check if the tumbling of the target can be detected by distant (ground based) photometric observations. In the following, we focus on detailed description of our model.

3.2   The model in detail

The input parameters—The target is a homogeneous triaxial ellipsoid in relaxed rotation state (or pure spin), i.e., rotating around the axis with the largest moment of inertia. It is described by following parameters: the mean radius of the body R_{m}, the semi axes ratios a/c and b/c ($a \geq b \geq c$), the body's bulk density ρ, the material strength (see Sect. 3.2.9 for more details), initial rotation period and whether the body is porous or not (see Sect. 3.2.9 for details on this). The projectile is a homogeneous sphere with diameter a d and the mean density δ. We do not take into account the rotation of the projectile since its angular momentum is a negligible contribution to the overall angular momentum budget.

The output—The overall description of the dynamical state of the target asteroid is given in an output file. It contains post-collision momentum and angular momentum vectors, inertia tensor, rotational axis misalignment angle β (as defined in Sect. 3.2.7) and a number of physical parameters from the calculation progress.

There is also a physical model of the body with the impact crater on its surface in a separate file. This physical model is then used for calculation of asteroid's ligthcurve after the collision. The program used and the process of lightcurve calculation is described more thoroughly in Section 3.2.10.

3.2.1   The coordinate system

We observe the impact in an inertial frame connected with the center of mass of the two bodies. The frame coordinate axes are identical to the principal axes of the target at the moment of impact (x in the direction of the target's longest axis, z in the direction of the shortest one).

The projectile is moving towards the target at a relative velocity $\boldsymbol{v}_{\mathrm{imp}}$ and hits it at the impact point I with spherical coordinates ϕ (longitude) and θ (latitude) on the surface of the target body. The prime meridian is defined as $y = 0$ and $x \geq 0$; together with the longest target axis it makes a common plane. See Fig. 3.1 for an illustration.

The impact speed is much greater than the target's escape velocity so we can neglect mutual gravity of the bodies and any curvature of the projectile's trajectory (Love and Ahrens 1996).

3.2.2   The crater shape

The geometrical representation of the crater is a paraboloid of revolution; this corresponds to the observations of simple impact craters on the Moon and other bodies in the Solar System (Chappelow and Sharpton 2002). The axis of the paraboloid is perpendicular to the local surface. We do not take into account border rim of the crater (which is usually present in real craters); we only model simple craters in our simulations. Complex impact structures can only be observed on the largest asteroids in the Main Belt and may be present on large icy bodies in the outer Solar System where the gravity plays a substantial role in crater formation (Leliwa-Kopystyński et al. 2008).
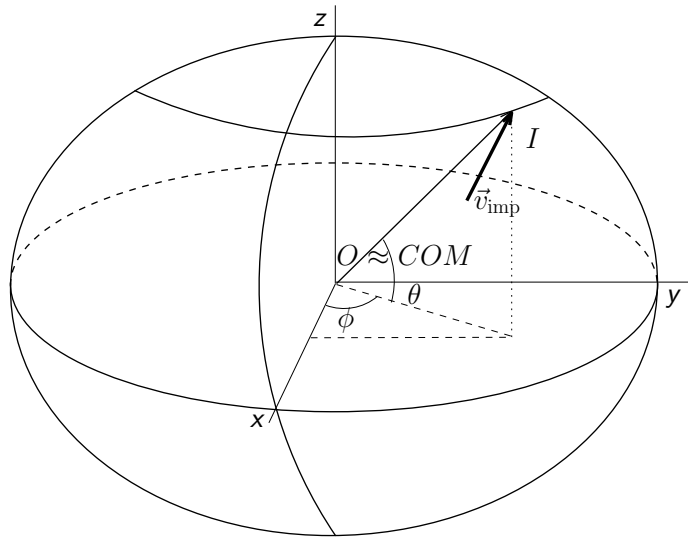
Figure 3.1   The coordinate system used in the model with origin at the center of mass (*COM*) of the two body system. It almost coincides with the target center of mass (*O*) for projectiles with $m_\mathrm{p} \ll m_\mathrm{t}$ (mass of the projectile and target, respectively). The coordinate axes x, y, z are identical to the principal axes of the target with smallest, intermediate and largest moment of inertia, respectively. The impact point I has the spherical coordinates ϕ (longitude) and θ (latitude), the projectile hits the target with the velocity $\boldsymbol{v}_\mathrm{imp}$, relative to the target.

3.2.3   Upper limit of the crater size

The diameter of the largest crater that a body of a given size can bear is calculated according to the relation in Burchell and Leliwa-Kopystynski (2010). They studied the maximum crater size on small bodies (asteroids, icy satellites, comets), which were imaged by space probes, and showed that it follows the relation

$$D = -(0.17 \pm 0.10) + (1.01 \pm 0.08)R_\mathrm{m}, \quad 0.7\,\mathrm{km} < R_\mathrm{m} < 120\,\mathrm{km}, \tag{3.1}$$

D being the crater diameter and R_m the target mean radius, both in kilometers.

The relative diameters of the impact craters $F = D/R_\mathrm{m}$, formed on the target in our simulations, were usually kept less than 1.26, which is the value for the largest crater on 253 Mathilde (Leliwa-Kopystyński et al. 2008). In some simulations we allowed for higher values of up to $F = 1.6$, since there is indirect evidence of the large crater on 90 Antiope (Descamps et al. 2009). However, conclusions based on this higher limit should be made with caution.

3.2.4   Dispersal and shattering criteria

For every collision, we calculated also its specific impact energy (kinetic energy of the collision per unit mass of the target). We compared it to the *dispersal criterion* as described by Stewart and Leinhardt (2012), who derived the dispersal criterion in gravity regime from their set of numerical simulations of collisions for wide variety of input parameters describing the colliding bodies. As *shattering criterion* we take 1/4 of the dispersal value according to Housen (2009). We plot our simulation results in a graph of specific impact energy vs. mean target radius (Fig 4.7) and discuss the results in Chapter 5.

3.2.5   Ejecta

The ejecta are assumed to leave the impact point with a cone-shaped velocity field symmetric around the line perpendicular to the surface at the impact point. We take this effect into account when calculating the angular momentum transfer efficiency (see Sect. 3.2.8 for detailed description and definitions).
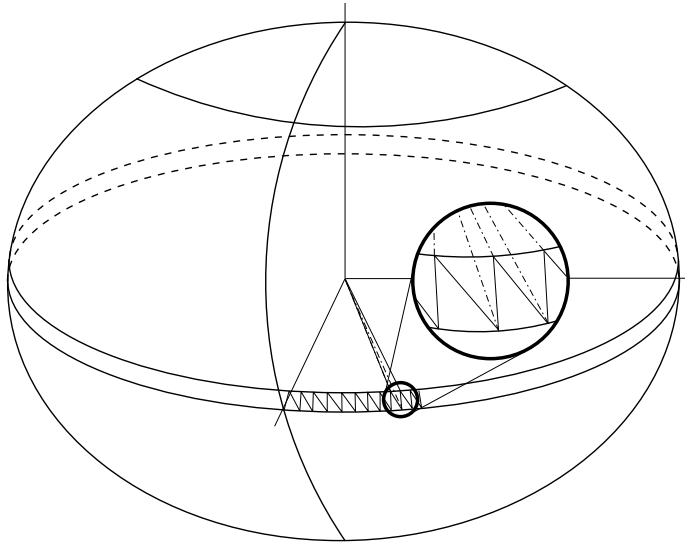
Figure 3.2   The formation of tetrahedra for inertia tensor calculation is illustrated. The
              surface is divided into triangular facets and together with the origin they form
              tetrahedra. The vertices of the facets are formed by iterating over the azimuth
              and latitude angles.

3.2.6   Inertia tensor calculation

The inertia tensor of the target before the impact is calculated analytically for the
body being homogeneous triaxial ellipsoid. The inertia tensor after the impact is
calculated numerically since the body is irregular – it is the triaxial ellipsoid with
the crater on its surface.

The body surface is divided into triangular facets and together with the origin
they form the tetrahedron (see Fig. 3.2). Its inertia tensor is calculated analytically
(see, e.g., Tonon 2004) and using the Steiner's parallel axis theorem it is translated
into the original center of mass coordinate system (target reference frame, origin
O). The inertia tensors of all such tetrahedra are then summed up and the inertia
tensor of whole body is obtained. Then it is translated to the new reference frame
with origin $O^\star$, since the center of mass has shifted due to the impact (see Eqn. 3.2).

The situation with facets covering the crater is only a bit more complicated.
First, the crater border is calculated. Then all the facets' vertices of the ellipsoid
surface inside this circular border are replaced with points of the paraboloid de-

scribing the crater floor. New facets' vertices are made of these points and the same procedure of tetrahedra inertia tensor calculation is used afterwards.

3.2.7   Principal axis deviation calculation

We try to find out, whether a subcatastrophic impact can create an observable excitation of rotation of the impacted body. The target's rotation was relaxed before the impact. This means it was rotating about the shortest axis, i.e., the axis with the largest moment of inertia for the homogeneous ellipsoid. We denote this moment of inertia I_3 and it holds that $I_1 \leq I_2 < I_3$.

An indication of the excited rotation will be a nonzero angle between the rotational angular momentum vector of the body after the impact $\boldsymbol{L}^\star$ and its shortest principal axis with the largest moment of inertia $I_3^\star$. The procedure of its calculation is as follows.

First, the inertia tensor of the target after the impact is calculated. Since the body possesses the impact crater, it lacks symmetry and the inertia tensor is calculated numerically.

Because the center of mass of the target $O^\star$ is shifted with respect to the original center of mass O after the impact, the resulting inertia tensor has to be shifted accordingly (the method calculates it with respect to O, hence it is not a central inertia tensor for the impacted body). We want to have the inertia tensor in a body frame (which is not inertial) with an origin in its center of mass, because then the components of this inertia tensor do not change with time as the body rotates. The transformation reads

$$\mathsf{I}_{ik}^\star = \mathsf{I}_{ik} + M(a^2 \delta_{ik} - a_i a_k), \tag{3.2}$$

where M is the total mass of the body, $\boldsymbol{a}$ is the center of mass shift vector (between O and $O^\star$), a is its magnitude, a_i and a_k are its Cartesian components and δ_{ik} is Kronecker delta (see, e.g., Kvasnica 1997).

Now we have to find the principal axes of the target after the impact. We can calculate them by finding the diagonal form of its inertia tensor, because they are determined by the eigenvectors of this tensor. The diagonalization is given by

$$\mathsf{I}_\mathrm{D} = \boldsymbol{Q}^\mathrm{T} \mathsf{I}^\star \boldsymbol{Q}, \tag{3.3}$$

where I_D is diagonal inertia tensor, $\boldsymbol{Q}$ and $\boldsymbol{Q}^T$ are orthogonal matrix and transposed orthogonal matrix, respectively. Its rows (and columns, respectively) are the eigenvectors of $\mathsf{I}^\star$.

In the next step we calculate the angular momentum vector just after the impact. We use the momentum conservation law

$$m_t\boldsymbol{v_t} + m_p\boldsymbol{v_{imp}} = m^\star\boldsymbol{v}^\star + \boldsymbol{P_{ejecta}}\,, \tag{3.4}$$

and angular momentum conservation law

$$\boldsymbol{L_t} + \boldsymbol{L_p} + \boldsymbol{L_{orb,t}} + \boldsymbol{L_{orb,p}} = \boldsymbol{L}^\star + \boldsymbol{L}_{orb}^\star + \boldsymbol{L_{ejecta}}\,, \tag{3.5}$$

where m_p is the mass of the projectile, $\boldsymbol{v_{imp}}$ is the projectile velocity vector, which for very low mass ratio of the projectile to target approaches the impact velocity, m_t and $m^\star$ are the masses, $\boldsymbol{v_t}$ and $\boldsymbol{v}^\star$ are the velocities of the target before and after the collision, respectively, and $\boldsymbol{P_{ejecta}}$ is the momentum of the ejecta. $\boldsymbol{L_t}$ and $\boldsymbol{L_p}$ are the rotational angular momenta of the target and the projectile before the impact, respectively, $\boldsymbol{L_{orb,t}}$ and $\boldsymbol{L_{orb,p}}$ are the orbital angular momentum vectors of the target and the projectile, respectively, with respect to the center of mass of the system, $\boldsymbol{L}^\star$ and $\boldsymbol{L}_{orb}^\star$ are the rotational and orbital angular momenta of the target after the impact, respectively, and $\boldsymbol{L_{ejecta}}$ is the angular momentum of the material ejected during the impact. Since the projectile was dissintegrated during the impact, all the quantities on the right sides of Eqns. 3.4 and 3.5 describe the post impact target body, and so we omit the subscript t .

The orbital angular momenta are calculated as

$$\begin{aligned}
\boldsymbol{L_{orb,p}} &= m_p(\boldsymbol{r_p} \times \boldsymbol{v_{imp}})\,, \\
\boldsymbol{L_{orb,t}} &= m_t(\boldsymbol{r_t} \times \boldsymbol{v_t})\,, \\
\boldsymbol{L}_{orb}^\star &= m^\star(\boldsymbol{r}^\star \times \boldsymbol{v}^\star)\,,
\end{aligned} \tag{3.6}$$

where $\boldsymbol{r_p}$, $\boldsymbol{r_t}$ and $\boldsymbol{r}^\star$ are the radius vectors of the projectile and the target before and after the impact, respectively, with respect to the system's center of mass. We calculate the target velocity before the impact as

$$\boldsymbol{v_t} = -\frac{m_p}{m_t}\boldsymbol{v_{imp}}\,. \tag{3.7}$$

Without an appropriate model of the ejecta, we need to, at least roughly, estimate its dynamical effect. We decided to use the efficiency of the linear (and angular) momentum transfer measured in laboratory impact experiments by Yanagisawa et al. (1996) and Yanagisawa and Hasegawa (2000) and we assumed that this relationship holds also for large scale impacts. Using the efficiencies η and ζ, the linear momentum transfer efficiency in normal and tangential direction with respect to the local surface at the impact point, respectively, we calculated the $\boldsymbol{v}^\star$ including the effect of ejecta. For the definition of these efficiencies and more detailed discussion see Section 3.2.8.

Finally we needed to describe $\boldsymbol{L_{ejecta}}$. For a small cratering impact, we can calculate the difference $\boldsymbol{L_{orb,p}} - \boldsymbol{L_{ejecta}}$ as

$$\boldsymbol{L_{orb,p}} - \boldsymbol{L_{ejecta}} = \eta m_{\mathrm{p}}(\boldsymbol{r_p} \times \boldsymbol{v_{norm}}) + \zeta m_{\mathrm{p}}(\boldsymbol{r_p} \times \boldsymbol{v_{tang}}), \tag{3.8}$$

where $\boldsymbol{v_{norm}}$ and $\boldsymbol{v_{tang}}$ are impact velocities in direction normal to and tangential to the local surface of the target, respectively.

The rotational angular momenta of the bodies are simply given by

$$\boldsymbol{L_t} = \mathsf{I_t}\boldsymbol{\omega_t} \qquad \text{and} \qquad \boldsymbol{L_p} = \mathsf{I_p}\boldsymbol{\omega_p}, \tag{3.9}$$

where we introduced inertia tensors of the target $\mathsf{I_t}$ and of the projectile $\mathsf{I_p}$ and angular velocities $\boldsymbol{\omega_t}$ and $\boldsymbol{\omega_p}$ of the target and the projectile, respectively.

When we put the equations 3.6, 3.7, 3.8 and 3.9 to the equation of angular momentum conservation 3.5, we can calculate the angular momentum vector of the target after the impact as

$$\boldsymbol{L}^\star = \mathsf{I_t}\boldsymbol{\omega_t} + \mathsf{I_p}\boldsymbol{\omega_p} + (\boldsymbol{L_{orb,p}} - \boldsymbol{L_{ejecta}}) + \boldsymbol{L_{orb,t}} - \boldsymbol{L_{orb}^\star}. \tag{3.10}$$

Finally we can calculate the angle between the rotational angular momentum vector of the target after the impact $\boldsymbol{L}^\star$ and the axis with the largest moment of inertia $I_3^\star$ (the axis is represented by unit vector $\boldsymbol{E_3}$, the eigenvector of the inertia tensor $\mathsf{I}^\star$). We denote this angle as β,

$$\beta = \arccos\left(\frac{\boldsymbol{L}^\star \boldsymbol{E_3}}{|\boldsymbol{L}^\star||\boldsymbol{E_3}|}\right). \tag{3.11}$$

The angle β is not constant, but it varies with changes of the principal vector $\boldsymbol{E_3}$ as the body precesses. We calculate the value of β right after the collision and we use

it as an approximate measure of the magnitude of tumbling displayed in lightcurve, for which the use of the instantaneous value of the misalignment angle is sufficient. This was checked by a set of simulations where we calculated the time evolution of β and we found that it is close to its maximum value just after the collision if it is not larger than about 65°.

3.2.8   Angular Momentum Transfer Efficiency

During the collision the projectile angular momentum is transferred to the target. The target body, however, does not obtain all of the angular momenta carried by the projectile, as shown by the experiments of small scale impacts (see, e.g., Yanagisawa et al. (1996), Yanagisawa and Hasegawa (2000) and references therein). A part of the angular momentum is carried away by high velocity ejecta and spall fragments and therefore we introduce the momentum transfer efficiency[1] defined as

$$\eta = \frac{m^\star v^\star_{\mathrm{norm}}}{m_{\mathrm{p}} v_{\mathrm{norm}}} \qquad \text{and} \qquad \zeta = \frac{m^\star v^\star_{\mathrm{tang}}}{m_{\mathrm{p}} v_{\mathrm{tang}}}, \qquad (3.12)$$

where $v^\star$ is the target speed after the impact, v is the projectile preimpact speed. The subscripts $norm$ and $tang$ denote the normal and tangential components to the target's local surface at the impact point, respectively. In our calculation, we use the experimentally obtained values of the efficiencies, but the thing is actually a bit more tricky.

From the impact experiments we see that the efficiencies depend on impact angle σ, which is an angle between the impact velocity vector and the line perpendicular to the surface at the impact point. The experimental results give the following dependencies

$$\eta(\sigma) = 1 + \eta_0 \cos^2 \sigma \qquad \text{and} \qquad \zeta(\sigma) = \zeta_0 \cos^2 \sigma. \qquad (3.13)$$

Yanagisawa and Hasegawa (2000) obtained the values of constants η_0 and ζ_0 at impact speed of $4\,\mathrm{km\,s^{-1}}$, which is close to the median impact speed between the Main Belt bodies ($\sim 5\,\mathrm{km\,s^{-1}}$, Bottke et al., 2005). For basaltic targets they give $\eta_0 = 1.52$

---

[1]The efficiency can be larger than one because backfire ejecta carries away some momentum in the direction opposite to the projectile course.
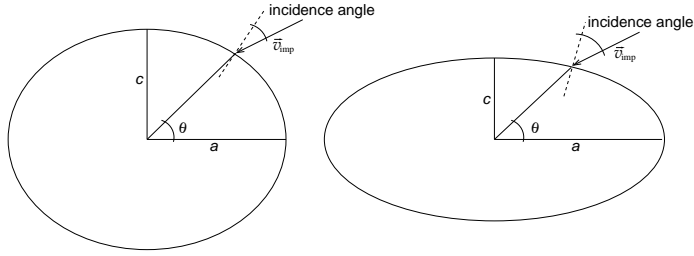
Figure 3.3   For two ellipsoids with different axial ratios a/c the same velocity vector $\boldsymbol{v}$ and impact point latitude θ result in different incidence angle of the projectile. Therefore the efficiencies η and ζ which are the functions of the incidence angle will be different for those two ellipsoids.

and $\zeta_0 = 0.409$. For sand target, which could be similar to a regolith-covered asteroid, Yanagisawa (2002) gives $\zeta_0 = 0.687$. He did not obtain the η_0 value and therefore he uses $\eta_0 = 0$ ($\eta = 1$) for an asteroid large enough to reaccumulate all the ejecta by its gravity. We follow this approach.

There is also a relation between the efficiencies and the shape of the target body as described in Yanagisawa (2002). It is sufficient to consider the equations given above since the impact angle σ is different for a sphere and an ellipsoid for the same impact velocity and therefore we get different values of η and ζ for different target shapes. This is illustrated in Fig. 3.3.

Recently the momentum and angular momentum transfer efficiency has been studied in laboratory experiments and also by theoreticians. Holsapple and Housen (2012b) and Housen and Holsapple (2012) presented the results of laboratory measurements of the momentum multiplication factor, in the literature usually denoted as β (do not confuse it with our angle β). It is a ratio of target post collision and projectile pre collision momenta magnitudes (similar to our η and ζ). It can be larger than one according to experimental results which are consistent with those of Yanagisawa et al. (1996) and Yanagisawa and Hasegawa (2000). It is mainly caused by the backfire ejecta momentum, which is added to the projectile momentum. It is important to say that only ejecta which escape the target after the collision contribute to this budget.

There is also a scaling effect which predicts that for larger asteroids the momentum multiplication factor or momentum enhancement can be much larger than one. It is indicated by collision experiments of Walker et al. (2012), who carried out

the collision of 4.45 cm aluminium sphere into two 1 m diameter granite spheres at $2\,\mathrm{km\,s^{-1}}$. Holsapple and Housen (2012a) gave a theoretical account to the momentum multiplication based on the analysis of dynamics of ejected material in their earlier paper (Housen and Holsapple 2011). The experimental results on this will be presented in a companion paper soon to be published.

Therefore, our model could be corrected by adopting the new experimental results and theoretical scaling of the momentum and angular momentum transfer efficiency in the collision. This is an opportunity to further develop this model.

This subject is not only important for the evolution of the asteroid rotations but it has also a practical meaning. One of the asteroid mitigation strategies is based on the use of kinetic impactor. It is a heavy spacecraft which collides with the asteroid and slightly changes its orbit so that it misses the Earth. The concept of such a mission should be soon verified by several space missions (Caltech JPL's ISIS, international project AIDA).

3.2.9   Scaling laws

To find out how large will be the crater formed on the asteroid, we followed the scaling laws of Holsapple (2003) and Holsapple (1993). The scaling laws, in general, predict the outcome of an experiment from another one with different values of problem parameters. When we study impact processes, we have results of centimeter scale impact experiments from the lab and we try to predict the outcome of the same experiment on a much larger (kilometer) scale.

The impact cratering scaling laws are based on an assumption that the projectile (which is much smaller than the resultant impact crater) behaves like a point source of momentum and energy (Holsapple and Schmidt 1987). The projectile charecteristics, size a, velocity U and density δ only affect the crater in a specific power law combination $C = a U^\mu \delta^\nu$. The exponent μ ranges from 1/3 to 2/3, which corresponds to momentum and energy scaling, respectively. The exponent ν is typically equal or close to 1/3.

Then there are two limiting regimes of the cratering, when either *gravity* or *material strength* dominates. For large lithostatic stress, the crater forms in *gravity regime* and the crater size decreases with increasing gravity or impactor size. If the

lithostatic stress $\rho\,g\,h$ is much smaller than the strength of the target material, gravity becomes unimportant and is neglected – this is a *strength regime*.[2]

There is a well established experimental method described, e.g., in Housen and Holsapple (2003), which is used to simulate the large scale impacts. This method uses a centrifuge which simulates much higher gravitational acceleration than on the surface of any asteroid or the Earth. It is based on *similarity* analysis as described in the following.

The dimensions of the crater in nondimensional form are expressed as

$$\frac{gD}{ga} = f\left[\frac{ga}{U^2}, \frac{Y}{\delta U^2}, \frac{\rho}{\delta}, n, \pi_{\mathrm{M}}\right], \qquad (3.14)$$

where g is the gravitational acceleration on the surface of the body at the impact point, D is the crater diameter, a is the projectile radius, δ its mass density, Y is a strength measure of the target material (depends on the specific impact process), ρ is the target density, n its porosity, U is the perpendicular impact velocity component and π_{M} is a set of other target material properties that affect the crater formation (except any size or time dependent properties).

Two impact events are similar, when all of the nondimensional ratios on the right side of the Eqn. 3.14 are the same for both events. It means that both events have the same target and projectile materials, the collision happens at the same velocity and the product ga is the same. Then, the value of gD is the same for two similar impacts. This is also true for other linear dimensions of the crater, such as depth or rim height. Therefore, the laboratory impact crater is similar to the large scale crater in its shape, the size and velocity distribution of ejecta etc. The scale of those two craters is equal to the ratio of the gravitational acceleration in the laboratory centrifuge experiment g_{C} (from normal gravity to several hundred G's, G is the gravitational acceleration on the surface of the Earth) to gravitational acceleration at the asteroid surface g_{A}.

For instance, the gravity at the surface of 253 Mathilde is $g_{\mathrm{A}} \sim 10^{-3}\,\mathrm{G}$ and the centrifuge experiment can be carried out at $g_{\mathrm{C}} \sim 500\,\mathrm{G}$, so the scale factor is $g_{\mathrm{C}}/g_{\mathrm{A}} = 5\cdot10^5$. The largest crater on Mathilde called Karoo has a diameter of $33\,\mathrm{km}$ and its formation is simulated by $\sim 7\,\mathrm{cm}$ crater in centrifuge experiment at $500\,\mathrm{G}$. If one wants to simulate smaller impact crater on that asteroid, he uses smaller acceler-

---

[2]Last two paragraphs are based on lucid explanation of the scaling laws in Housen and Holsapple (2003).

ation in the centrifuge. A $1\,\text{km}$ crater on Mathilde would be simulated by $\sim 10\,\text{cm}$ crater at $10\,\text{G}$.

Based on shapes of simple craters on the Moon and other Solar System bodies, we decided to model the impact crater as paraboloid of revolution. We assume that the aftermath of the crater formation (e.g., a collapse of the crater walls) does not have a substantial dynamical effect (the mass redistribution is small).

The radius and depth of the crater are given by the following formulae

$$R_c = K_r V_c^{1/3} \qquad \text{and} \qquad D_c = K_d V_c^{1/3}, \tag{3.15}$$

where K_r and K_d are the shape constants specific for a material of the asteroid (Holsapple, 2003) and V_c is the volume of the crater given by

$$V_c = \frac{4\pi d^3}{3}\frac{\delta}{\rho}\pi_V, \tag{3.16}$$

d being the impactor diameter, δ its density, ρ is the target's density and π_V is given by

$$\pi_V = K_1 \left\{ \pi_2 \left(\frac{\rho}{\delta} \right)^{(6\nu-2-\mu)/3\mu} + K_2 \left[\pi_3 \left(\frac{\rho}{\delta} \right)^{(6\nu-2)/3\mu} \right]^{(2+\mu)/2} \right\}^{-3\mu/(2+\mu)}$$

$$\pi_2 = \frac{g\,d}{U^2}, \quad \pi_3 = \frac{\bar{Y}}{\rho\,U^2}. \tag{3.17}$$

Parameters K_1 and K_2 and exponents μ and ν come from laboratory impact experiments (Holsapple 1993), g is the gravitational acceleration at the impact point, U is the impact velocity component perpendicular to local surface and $\bar{Y}$ is the target's material strength.

In the model, we assume effective strength for the excavation, because the shock wave fractures the body during the early phase of the impact. As the body becomes porous, this effective strength can actually increase as the impact energy transfer is hindered (Binzel et al. 2003). The effective strength is related to the most important cratering process at work for a specific impact (say, to the very porous material versus solid rock). It can be tensile, shear or other material strength that can be measured in laboratory but also some more complicated combination of those measures; for details see Richardson (2009), Nolan et al. (1996) and Holsapple (2007).

Table 3.1   Scaling and material constants for non-porous and porous body materials.

Material	K_1	K_2	μ	ν	$\bar{Y}$(MPa)	ρ (g cm^{-3})	K_r	K_d
Rock	0.095	0.257	0.55	0.33	10	2.0	1.1	0.6
Lunar regolith	0.132	0.26	0.41	0.33	0.01	1.5	1.4	0.35

Table 3.2   Physical parameters of the sample target bodies.

Figure	target mean diameter [km]	initial rotation period [h]	β [deg]
3.4	144.2	32	4.2
3.5	36.1	32	11.5
3.6	1.4	2	15.5
3.7	7.2	12	18.8
3.8	7.2	22	34.3

Speaking of porosity, in our simulations we consider two cases: a rocky material corresponding to macroscopically non porous bodies and lunar regolith for porous asteroids. For the values of scaling and material constants we use, see Table 3.1. Note that even rocky material may include some level of microporosity.

3.2.10   Synthetic lightcurves

We generated rotational lightcurves for the resulted model bodies. We used the program written by Mikko Kaasalainen (Kaasalainen 2001) and modified by Josef Ďurech (2011, pers. communication), which generates the rotational lightcurve for an arbitrarily shaped body with given dynamical parameters. The shape is given by a set of oriented triangles building up the body surface mesh, the light scattering law was that of Hapke (Bowell et al. 1989). The input also includes the orientation of axis of rotation at some instant of time as well as the Euler angles for that instant that determine the body's orientation in space.

The Euler equations of motion are then solved and the integral light flux is calculated for given observational geometry with a chosen time increment. We simulated real observations with varying time sampling rates to avoid alias effects in generated lightcurves and we also added a Gaussian noise.
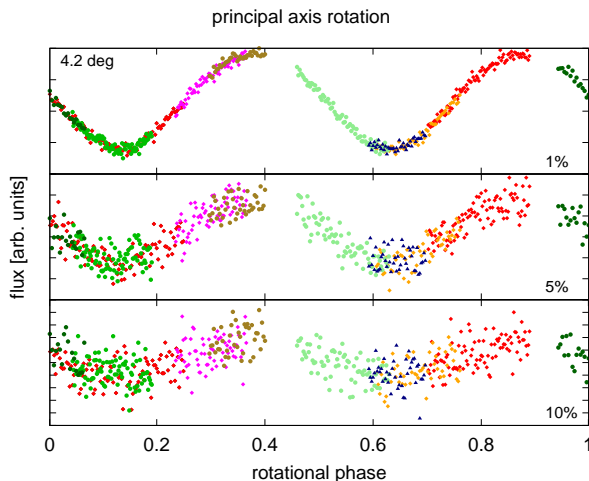
Figure 3.4   A lightcurve of a body impacted by a small projectile, $\beta = 4.2°$. The horizontal axis is the rotational phase, the vertical axis is a light flux normalised to unity. It is undistinguishable from a lightcurve of principal axis rotator even in lowest noise case.

A blind test lightcurve analysis was done for a set of cases with increasing β to find out if the tumbling is detectable in the synthetic lightcurve. In Figs. 3.4–3.8 we present five sample lightcurves with three levels of noise – 1%, 5% and 10% of the mean flux value. The axial ratios of the target were $a/c = 2.0$ and $b/c = 1.5$. The diameter of a projectile was about 5% of the mean diameter of the target body in all these simulation runs. Other parameters describing the target body are in Table 3.2.

The values of rotation axis misalignment for which the tumbling is clearly detected start at $\beta \sim 15°$, although for less accurate data β has to be higher by 5–15 degrees depending on the noise level of the lightcurves. If the best period solution does not fit the data 'nicely' and the residua are higher than expected from the inherent accuracy of the data, lower noise data are needed to check if the asteroid is tumbling or not. The detectability of tumbling in distant or in situ photometry for different excitation magnitude, the mode of free precession (SAM versus LAM) and the accuracy of the data is an interesting problem and it will be subject of our future research.
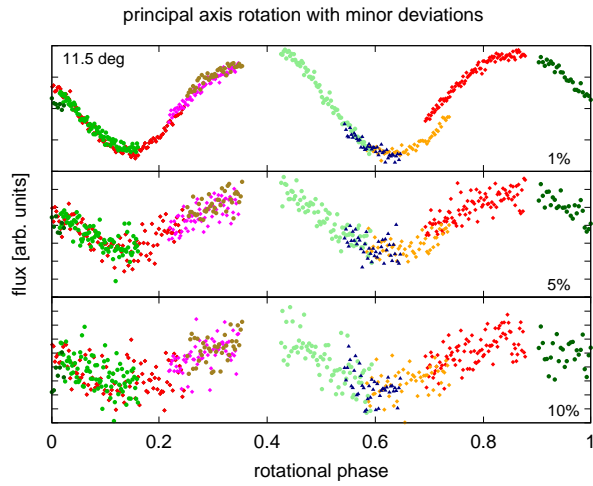
Figure 3.5   A lightcurve with apparent minor deviations from single periodicity, $\beta = 11.5°$, only marginally distinguishable by photometric observation with most accurate measurements. Otherwise, the deviations are washed down by the noise.
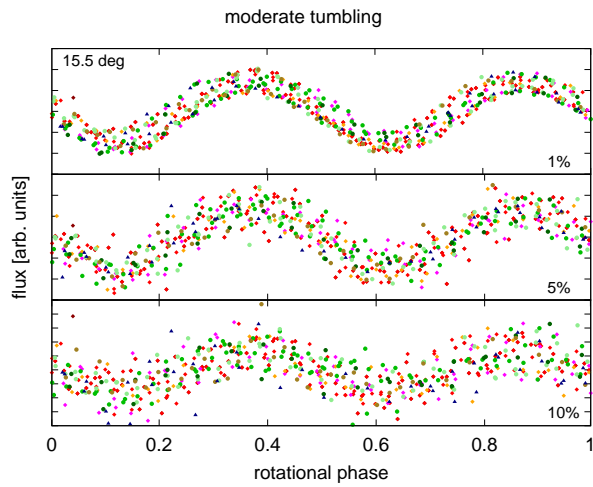
Figure 3.6   A moderate tumbling signal is apparent in this lightcurve for the lowest noise level, $\beta = 15.5°$.

Figure 3.7   In this lightcurve the tumbling is evident even for moderately noisy data, $\beta = 18.8°$.

Figure 3.8   Obvious tumbling for this slowly rotating body, $\beta = 34.3°$. It should be detected even in low quality datasets.

3.3   Model limitations and adopted approximations

Here we discuss our model limitations and describe also more deeply the approximations we use to simulate the impact crater formation on asteroid surface and its dynamical effects.

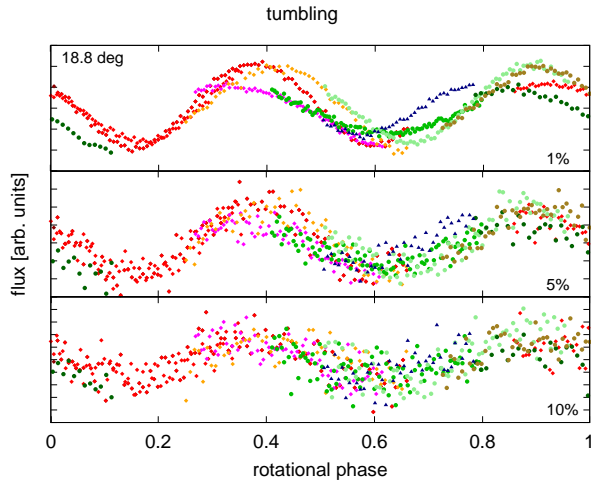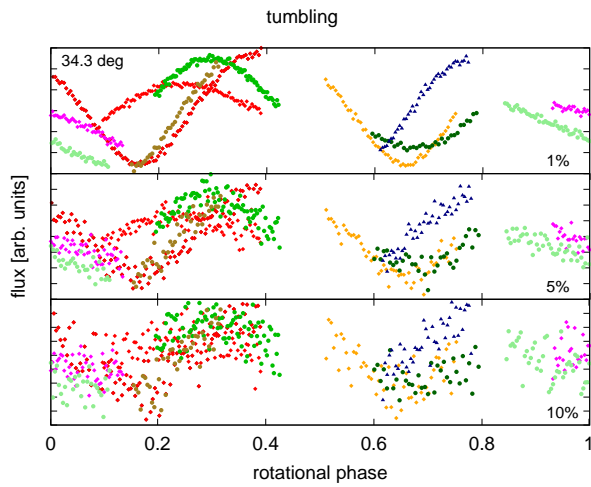For the calculation of the impact crater dimensions we use the scaling laws for impact cratering, which connect small scale laboratory experiments and large scale collisions we are interested in. These scaling laws, however, only hold under certain assumptions. They were derived for a halfspace target with the projectile small enough, so that point source (of energy and momentum) approximation holds. It seems to be true for small to moderate incidence angles, but it is not usable for very oblique impacts. Therefore, we limit all our simulation runs to maximum incidence angle of 50°. For incidence angles larger than 0° the impact velocity component perpendicular to the surface at the impact point is used. We also limit the impact speed to values higher than $1\,\mathrm{km\,s^{-1}}$ as for lower speeds the scaling laws do not apply (Holsapple 1994).

As an input for the scaling laws we use two sets of material constants. These include density and strength of the target body material. We use the sets of those constants for rocky material and lunar regolith (see Table 3.1). These may be closest analogues of the asteroid material for which we have its material constants measured but we cannot be sure it is true. In 2010, probe Hayabusa of Japan Aerospace Exploration Agency succesfully returned asteroid dust to Earth. There are several more sample return missions planned to visit an asteroid, e.g., Hayabusa 2 and NASA's OSIRIS-REx. These missions can give us more constraints on the material properties.

The description of the porosity, which is an important mechanical property of the asteroids, is very limited in our model. Basically we only change the constants in scaling laws which yields different dimensions of the impact crater. Housen and Holsapple (2003) showed that porosity has substantial effect on the amount of ejecta and this will obviously display in the momentum and angular momentum exchange between the projectile and the target. The porosity can also have some influence on the crater shape and its depth to diameter ratio as shown by recent impact experiments into pumice targets (Flynn et al. 2013, pers. communication –

CD8 workshop talk). More work needs to be done to include porosity description more thoroughly into our model.

There is also another regime of impact cratering which is valid for highly porous materials and therefore it can be valid for many real asteroids. It is a compaction mechanism described by Housen et al. (1999). They showed that this mechanism is able to explain the lack of ejecta around the huge impact craters and also close packing of those craters[3] on the surface of 253 Mathilde, large C type slowly rotating tumbler with a porosity of some 50% (Veverka et al. 1999). This mechanism has a different effect on the dynamics of the asteroid at least from two points of view: first, it changes the density of the material underneath the crater (the material is pushed into the pores during the collision) and second, it dramatically changes the dynamics of the ejected material (see the previous paragraph) and therefore the momentum imparted to the target. Also this mechanism will be the subject of our future research.

Shapes of real asteroids are very diverse as they are influenced by collisions, tidal effects and rotational fission potentially causing landslides and also other changes of their surface and overall structure. We only modeled the target bodies as triaxial ellipsoids which is usually the first approximation of asteroid shapes. In the future, we would like to use also irregularly shaped bodies in our model to see its effect on the results. However, we remind the reader that cratering into irregularly curved surface is still beyond the capability of the present scaling laws.

We use triaxial ellipsoids as targets in our model and so we assume the scaling laws are usable even for the curved surface. It is probably true for small craters, for which the curvature is not large, but is is questionable for larger craters comparable to the size of the target. Some observational constraints on this can be found in Leliwa-Kopystyński et al. (2008). The only experimental results of this effect are those of Fujiwara et al. (1993) who describe that craters formed on a curved surface are larger than those on flat surface and when the curvature of the impacted surface is comparable to the crater radius (on the flat surface), the crater size sharply increases and becomes convex rather than concave (after Housen and Holsapple 2003).

Our model is analytic, it is not a numerical simulation of the collision. We do not model any processes that occur during the collision or afterwards. The impact

---

[3]Some of them basically overlap and yet the older one is not damaged by the newer one.

crater is formed on the surface of the target and we only calculate its dimensions by scaling laws. The calculation of dynamical effect of the ejected material is based on the laboratory experiments of hypervelocity collisions mentioned in Section 3.2.8.

Although we considered the rotation of the target body in the angular momentum conservation law, there are probably other parts of the model that could be affected by the rotation.

First, rotation seems to change the amount of ejected material. Faster rotation increases the mass of ejecta (Richardson et al. 2013, pers. communication – CD8 workshop talk). Moreover, for larger asteroids the collsional ejecta escapes preferentially in the direction of rotation which can reduce their spin – this is called angular momentum drain (Dobrovolskis and Burns 1984).

Second, the laboratory impact experiments suggest that rotating asteroid might fragment more easily for near catastrophic collisions (Morris et al. 2013, pers. communication – CD8 workshop talk). Also the experiments of Housen (2004) show a strong dependence of the dispersal criterion $Q^\star$ on the rotation rate in the strength regime of collision. This dependence is not understood yet and also it is not clear if the similar relationship exists in gravity regime. On the contrary, N-body simulations of Takeda and Ohtsuki (2009) showed no evidence that asteroid's intial spin would change the energy needed to disrupt the body.

Third, we speculate that in gravity regime of collisions, the target rotation should be included in the calculation at least for fast rotators. The effective acceleration (gravitational plus centrifugal) should be used in scaling laws for calculating the impact crater dimensions. To our knowledge, there has been no paper on this subject.

In our model, the bodies moved in a line before the collision. The impact speeds were much higher than their escape velocities, therefore we did not take into account neither gravitational focusing nor tidal effects (Love and Ahrens 1996).

The next chapter resumes the main results of our present research. We show the sensitivity of the excitation of rotation to various input parameters describing the colliding bodies. In Section 4.2 we then show that the value of β is closely related to $L_{\mathrm{orb}}/L_{\mathrm{t}}$ ratio independent of other parameters describing the two bodies. This result gives us a tool to quantitively judge the dynamical outcome of a subcatastrophic collision with regard to the rotation of the target asteroid.

4

Results

In this chapter we present the results of our simulations. In individual runs, we varied one or two input parameters (e.g., body size or its rotation period) while keeping other constant. Then we plotted graphs showing the relationship between the varied parameters and the misalignment angle β of the angular momentum vector after the collision (see Section 3.2.7). Presented graphs do not show results of all our simulations, but rather a representative sample.

4.1 Rotation axis misalignment

The following sections give the graph displaying the dependency of rotational axis misalignment β on a specific physical parameter of the target or projectile and its detailed description. Then we interpret the dependencies usually by the dimensional analysis. The constant parameters describing the body in these runs were $a/c = 2.0$, $b/c = 1.5$, $\bar{Y} = 10\,\mathrm{MPa}$, bulk densities of the target and the projectile were $2\,\mathrm{g\,cm^{-3}}$. The projectile collided with the body at $v_x = -5\,\mathrm{km\,s^{-1}}$ and the impact point coordinates were $\phi = 15°$ and $\theta = 15°$. The incidence angle for such geome-

try is approximately 35°, which is ten degrees less than the statistical average for a spherical target body (Love and Ahrens 1996).

4.1.1   Target's rotation period

Figure 4.1 shows the misalignment of the angular momentum (AM) vector for various values of the initial rotation period and four body sizes. As expected, β increases with increasing rotation period. The slower rotation of the target implies it has a lower angular momentum L_t and therefore the projectile with a given orbital angular momentum L_{orb} will excite the body more.

We can clearly see that even for the largest body the tumbling could be detected for periods longer than about 42 h. To understand qualitatively this graph, we can use dimensional analysis. For the rotational angular momentum of the target and for the orbital angular momentum of the projectile, respectively, we have

$$L_t \sim I_t \omega_t \sim m_t r_t^2 \omega_t \sim r_t^5 \frac{2\pi}{P_t},$$

$$L_{orb} \sim r_t m_p v_{imp}, \tag{4.1}$$

where r_t is the mean target radius and P_t is the target's period of rotation. The ratio of these two is

$$\frac{L_{orb}}{L_t} \sim \frac{P_t}{r_t^4}. \tag{4.2}$$

It means that the smaller the target and the longer the period of rotation, the higher the ratio of the angular momenta and therefore higher β.

4.1.2   Projectile size

In another run, the sampled parameter was the projectile size. The results are plotted for small body both porous and non-porous (Fig. 4.2). As the relative projectile size increases, β also increases. A larger projectile makes a larger crater on the target body and hence a larger change of the inertia tensor.

The parameters describing the impact were the same as above, the mean body diameter was 1.4 km and its intial rotation period was 32 h. For a porous target, there is a different set of the scaling and crater shape parameters as described in
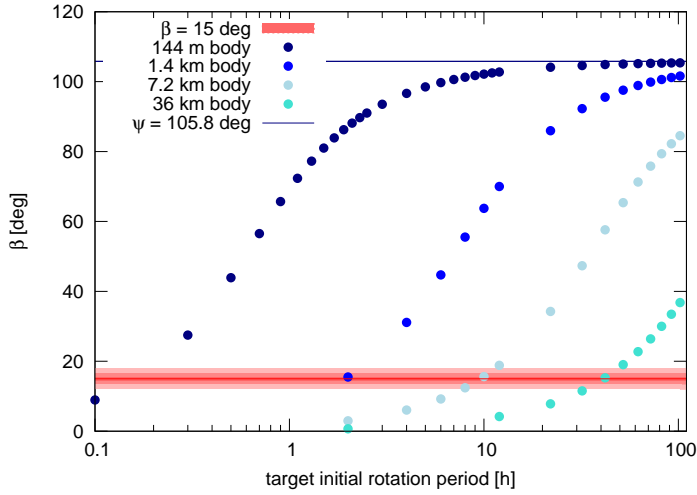
Figure 4.1   A relationship between the AM vector misalignment and the initial rotation period of the body, for four different sizes. The projectile size was adjusted so that it excavated a crater of maximum size (see Section 3.2.3). Details in Sect. 4.1.1

Section 3.2.9 and a different cratering efficiency (see Section 3.2.8). There are only subtle differences of at most two degrees in β between porous and non-porous targets. Note that this difference does not have to be realistic as the physics of the impact into a porous material is probably more complicated and not well understood yet. In future, some numerical simulation will be useful to describe this process more thoroughly and more realistic.

4.1.3   Target strength

In Fig. 4.3, we plot the strength–misalignment relationship for a small and a moderate size body. For increasing target strength there is an increasing threshold crater size (see Section 3.2.3 for details). We kept the actual crater size near the threshold, so for larger target strength we had larger projectile with larger L_{orb} (L_t being constant).

Other parameters than the strength and the body sizes (144 m and 7.2 km, respectively) were the same as in previous experiment, the initial rotation period was 32 h.
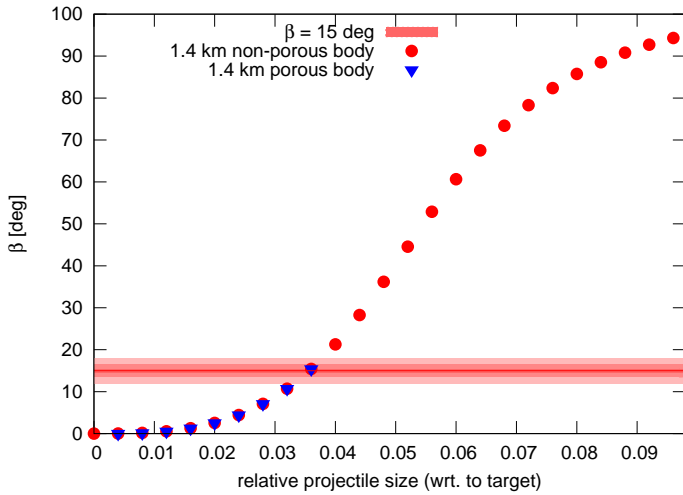
Figure 4.2 A relationship between the AM vector misalignment and the projectile size for small target with 32 h rotation period. The simulation for non-porous and porous body. Details in 4.1.2.
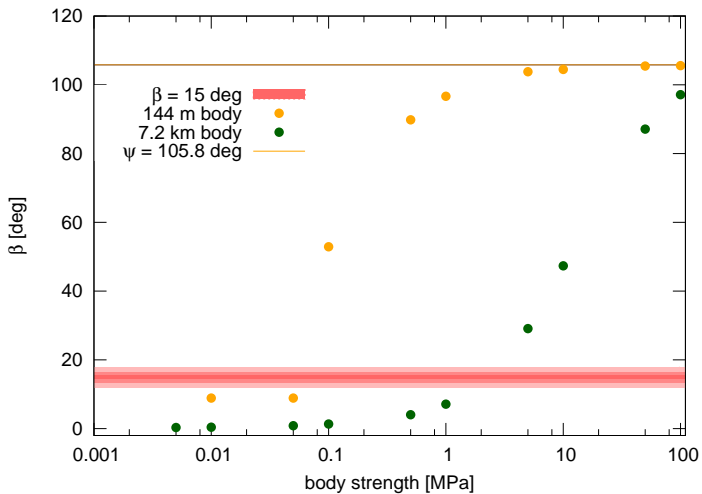
Figure 4.3 A relationship between the AM vector misalignment and strength of the small and moderate size target. Details in Sect. 4.1.3.
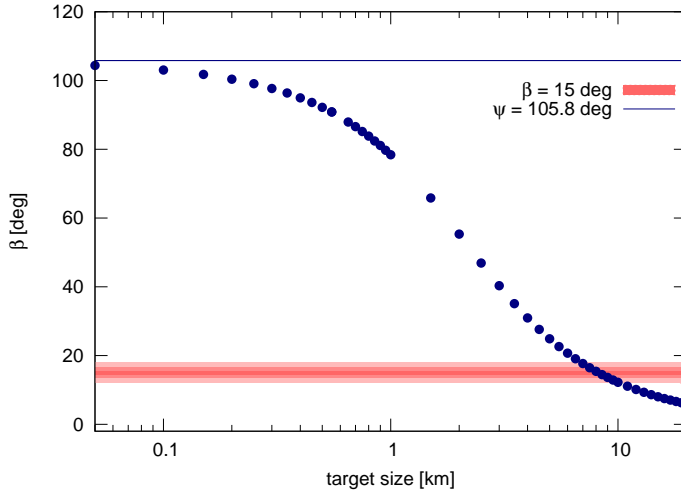
Figure 4.4   A relationship between the AM vector misalignment and target size. Details
in 4.1.4.

4.1.4   Target size

The last run shows a dependence of the misalignment on the target size, see Fig. 4.4.
It is clearly seen that with decreasing target size β increases. As before, it was caused
by increasing $L_{\mathrm{orb}}/L_{\mathrm{t}}$ ratio, which can be, again, explained by dimensional analysis
(see Eqn. 4.2).

4.2   Angular momenta ratio

Here we show, that the results of all our simulations can be described by a ratio of
the projectile orbital to target rotational angular momentum $L_{\mathrm{orb}}/L_{\mathrm{t}}$. The relation-
ship can be approximately described by the formula

$$\cos\beta = \pm \left[1 + \frac{\sin^2\psi}{(L_{\mathrm{t}}/L_{\mathrm{orb}} + \cos\psi)^2} \right]^{-1/2} , \qquad (4.3)$$

where the $+$ sign is for $L_{\mathrm{t}} \geq -L_{\mathrm{orb}}\cos\psi$ and $-$ sign is for $L_{\mathrm{t}} < -L_{\mathrm{orb}}\cos\psi$, ψ is
the angle between the two angular mometum vectors just before the collision. For
derivation of this formula see Appendix A.
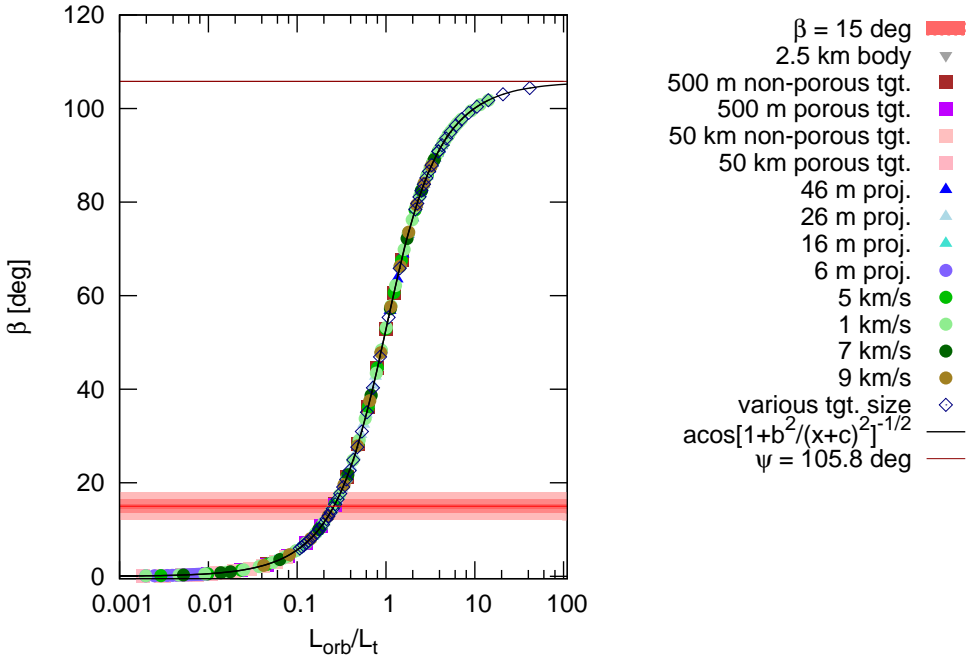
Figure 4.5 The results of all presented simulations included in one graph as a function of $L_{\mathrm{orb}}/L_{\mathrm{t}}$ (points, see the key for their description). The black solid curve is β as a function of $L_{\mathrm{orb}}/L_{\mathrm{t}}$. The angle between those AM vectors ψ was constant for all the simulations and the curve converges to its value of $105.8°$.

We plotted all the simulation results in Fig. 4.5 together with the curve given by Eqn. 4.3.

There is another obvious feature in the above mentioned graph – the values of β converge to the value of ψ. This is to be expected when the ratio of the magnitudes of these two vectors becomes much greater than one

$$\frac{L_{\mathrm{orb}}}{L_{\mathrm{t}}} \gg 1 \qquad \cos\beta = \left[1 + \frac{\sin^2\psi}{(L_{\mathrm{t}}/L_{\mathrm{orb}} + \cos\psi)^2}\right]^{-1/2} = \left[1 + \frac{\sin^2\psi}{\cos^2\psi}\right]^{-1/2} = \cos\psi.$$

$$(4.4)$$
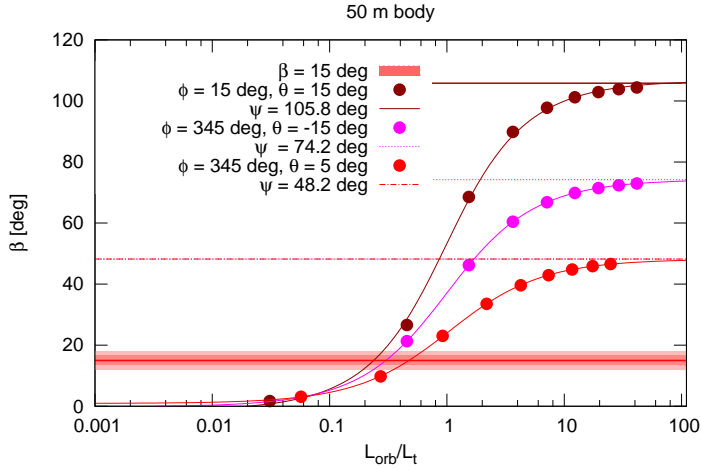
Figure 4.6   Test of β convergence to ψ for various impact geometries (the angle between L_t and L_{orb} vectors). See text for details.

If, on the contrary, the L_{orb} is negligible when compared to L_t, we obtain the obvious result

$$\frac{L_{orb}}{L_t} \ll 1 \qquad \cos\beta = \left[1 + \frac{\sin^2\psi}{(L_t/L_{orb} + \cos\psi)^2}\right]^{-1/2} = 1 \qquad \beta = 0. \qquad (4.5)$$

We have checked this convergence of β to ψ also for other angles (other impact geometries) and the results are presented in Fig. 4.6. The target was 50 m body with other parameters as in previous simulations and the projectile collided with it at $v_x = -5\,\mathrm{km\,s^{-1}}$. The impact point coordinates are described in Fig. 4.6 by ϕ and θ (see Section 3.2.1 and Figure 3.1).

4.3   Dispersal and shattering criteria

It is important to compare the specific energy of every collision with some energy threshold criterion so that the collision is subcatastrophic (cratering regime) and does not cause substantial damage to the target. *Dispersal criterion* is the specific energy required to disperse half the total mass of the target and the projectile. Usually it is denoted Q_D^*. The *shattering criterion*, Q_S^*, is the kinetic energy of the projec-

tile per unit target mass such that half the target mass remains intact (Stewart and Leinhardt 2009). For the strength regime, these two criteria are esentially the same but in gravity regime they can differ substantially.

Now, we compare the energy of our collisions with even lower energy threshold as described by Housen (2009). This is the minimum energy per unit target mass to produce large scale damage in a target body, Q^*_{LD}. In the calculation of the criterion, we followed Stewart and Leinhardt (2012). They simulated collisions in gravity regime with wide variety of input parameters describing the colliding bodies. As the large damage threshold we take 1/4 of the previous value according to Housen (2009).

In Fig. 4.7, we plotted specific impact energy as a function of the mean target radius and calculate the Q^*_{LD} criterion for most collisions we simulated. Since the diversity of dispersal or shattering criteria in literature is rather high, we plot other such functions in that figure for comparison to our choice. For review on these criteria see for instance Holsapple et al. (2002) and Benz and Asphaug (1999). The thorough description of the dispersal criterion in gravity regime based on large set of numerical simulations can be found in Leinhardt and Stewart (2012).

We considered targets with various dimensions but constant $a/c = 2.0$, $b/c = 1.5$, with a rotation period of 36 h, mean density 2 g cm^{-3} and strength 1 MPa. The projectiles were of various sizes, their density was 2 g cm^{-3} and the impact speed was $v_x = -5$ km s^{-1}. The impact point coordinates were $\phi = 21°$ and $\theta = 21°$, the incidence angle for such geometry is approximately 44°.

We also plot the limiting value of the specific energy for which the tumbling after the collision becomes detectable in the lightcurve as described in Section 3.2.10. For its derivation see Appendix B. The bodies, for which the specific impact energy of the collision was less than this limiting value, are labeled 'not tumbling' for simplicity but this label implies that the tumbling would not be detected in their lightcurves. If the collision energy exceeds the Q^*_{LD} criterion, we label the resulting body 'tumbling but shattered' and we mark it with different symbol (×) in the graph.

We plotted an upper limit of the specific impact energy with dashed line in the graph. It corresponds to the ratio of the diameter of the largest crater to the mean target radius $D/R_{\text{m}} = 1.26$ (the largest known crater on 253 Mathilde). This line gives us the idea on what are the largest craters observed on the surfaces of small bodies in the Solar System.
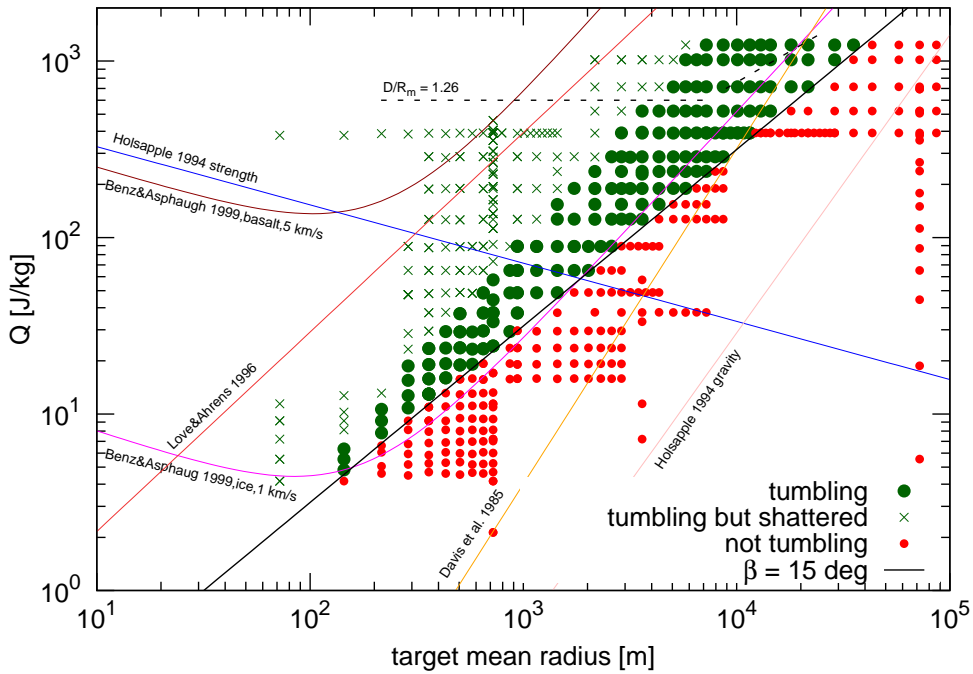
Figure 4.7   The specific energy of collision as a function of the mean target radius. Small red circles denote bodies for which the tumbling was not apparent in the lightcurve. Large green circles are tumbling bodies which did not exceed the Q^*_{LD} criterion. Green cross symbols are for bodies that were seriously damaged, shattered or even had a half of its mass dispersed by the collision. The dispersal criterion is according to Stewart and Leinhardt (2012). Other dispersal or shattering criteria are also displayed. The thick black line is the limiting specific impact energy as derived in Appendix B. See text for details.

5
Conclusions

In the present research we focused on the plausibility of the collisional origin of the excited rotation of asteroids. We constructed an analytical model, described in Chapter 3, to investigate this process and we obtained the following main results.

We found that large subcatastrophic collision is physically plausible process to excite the asteroid rotations. We measure the strength of the excitation by the rotational axis misalignment defined as an angle between the shortest principal axis of the asteroid and its rotational angular momentum vector and we denote this angle as β. The excited rotation (or tumbling) is detectable by distant photometry for $\beta \gtrsim 15°$ with photometric data with accuracy of 1% and for $\beta \gtrsim 30°$ with data of 10% accuracy.

We tested the sensitivity of the excitation of rotation to several parameters describing the target, the projectile or the collision circumstances. We found that the result can be described simply by the ratio of the orbital angular momentum (mainly carried by the projectile) and the rotational angular momentum of the target. We derived a simple relation between this ratio and the angle β, see Eqn. 4.3 in Sect. 4.2. This relation can be used for evaluation of the rotation excitation in a subcatastrophic collision.

We also compared the specific impact energy in every simulation run to the threshold energy which would cause a serious damage of the target asteroid. We found that asteroids as small as $\sim 100\,\mathrm{m}$ can have excited rotations by collisions without being damaged. This limit depends upon a choice of the threshold energy for large damage of the asteroid; details on this are in Sect. 4.3.

To investigate a relevancy of the collisional mechanism in rotational dynamics of asteroids, it is necessary to construct a more complex model. We have only proven that collision *can* be responsible for tumbling but it is not sufficient to say that collisions *are* the mechanism causing tumbling. Vokrouhlický et al. (2007) showed that YORP can slow down the rotation of the asteroid to a very slow spin but not to complete halt. Eventually, this leads to onset of chaotic tumbling which, after some time, ends up in rotation state with a regular motion of the spin axis in the body frame (free precession). This evolution is, however, limited by collisions powerfull enough to change the asteroid spin state. Therefore, the updated model should follow the similar procedure described in Vokrouhlický et al. (2007), but it should include collisional excitation.

The evolution of spins of small Main Belt asteroids was modeled by Marzari et al. (2011) who included both, YORP and collisions, and obtained a better match with the observed population when compared to models which included only YORP. It would be useful to carry out similar simulation specifically focused on tumbling.

6
Further work

In our further work, we will improve our model in order to remove its limitations and find better approximations. These were described in Sect. 3.3 and we will only briefly repeat it here. Furthermore, we will concentrate on more general plans that will include our model.

We will work on improving the description of porosity in our model as it is a very important characteristics of many asteroids and it plays a substantial role in collisions. Housen and Holsapple (2003) showed that porosity affects the amount of ejecta and this also propagates to the efficiency of angular momentum transfer from the projectile to the target. The porosity can also change the shape of the impact crater and its depth to diameter ratio (Flynn et al. 2013, pers. communication – CD8 workshop talk) which affects the inertia tensor and therefore the strength of the excitation of rotation.

We will add the compaction mechanism of cratering described by Housen et al. (1999)) because it is a preferable cratering regime for highly porous asteroids such as 253 Mathilde (Veverka et al. 1999). This will require a more extensive change of the present model and it can bring substantially different results. It could give us more realistic constraints on the efficiency of the collisional excitation of rotation for very porous asteroids.

Triaxial ellipsoids are widely used as the first approximation of asteroid shapes in various theoretical models. We also used this shape but we plan to extend the model for irregular bodies. There are several tens asteroids for which we have 3D shape model mostly based on radar observations. It may be interesting to test the dependancy of our model outcomes on the shape of the body used in the model. Note, however, that the effect of the curved surface on the formation of the impact crater is not well known yet. It is one of the problems that should be addressed by a future research of the impact processes.

In the present research, we described the outcomes of the subcatastrophic collisions depending on various input parameters of the colliding bodies and the collision itself. It would be useful to run randomized simulations for a specific asteroid population to find average rotational axis misalignment caused by collisions. This could be incorporated into models tracking the evolution of the asteroid rotations as the zeroth approximation.

Stepping further, the evolution of asteroid rotations could be simulated in a more complex way to also include the collisional excitation as follows. The model should include the most important dynamical processes that affect rotation of asteroids, i.e., collisions and Yarkovsky–O'Keefe–Radzievskii–Paddack (YORP) effect. While the collisions cause an instantaneous change of the rotation, YORP works on long timescales. Large collisions can be either catastrophic, leading to asteroid dispersal, and collisional fragments may be in a state of excited rotation as suggested by experiments of Giblin and Farinella (1997). Or they can be subcatastrophic that can spin up or spin down the target and also lead to excited rotation, sometimes large enough to be observed in the asteroid's lightcurve.

The effects of subcatastrophic impacts are an important part of the dynamical evolution of asteroid rotations. They affect the rotation of asteroids directly but also indirectly by, e.g., changing some of the surface properties with respect to sunlight re-emission and therefore influencing the magnitude and possibly the sign of the YORP torque (Statler 2009).

When considering collisions, we have to calculate or at least estimate the probability of collisions for a specific asteroid. The collisional excitation of rotation is more effective for smaller asteroids with slower rotation. Therefore, a sufficient collision can be caused by a rather small projectile (say, a few per cent of the target diameter). The problem is that the number of such bodies in the Main Belt or other group of asteroids is only estimated by extrapolation of the observed population.

For small asteroid counts we suppose the power law relation with lower exponent than for the moderate size (Ivezić et al. 2001).

Moreover, it is necessary to consider the damping of the excited rotation to find out how long can be observed the excited rotation from the last large collision. Also observational biases need to be estimated for observational methods (e.g., optical photometry) to estimate the population of tumbling asteroids. Only then we can compare the output of the simulated population of tumbling asteroids to the observed sample.

To learn more about the origin of tumblers and processes causing the excitation of their rotation, we can follow this procedure. Consider the population of asteroids, say, in the Main Belt of several tens of thousand bodies. We let this population evolve in time by the means of monte carlo numerical method. We include all the above mentioned processes into our simulation. The results of such simulation will serve as a base for estimating of the probability to observe an excited asteroid, which can be compared to the actual observations.

Since our model is analytical and includes several approximations, it would be very useful to investigate the effect of subcatastrophic collisions on the asteroid rotations also by another method. The most obvious choice would be the smooth particle hydrodynamics model (SPH; Benz and Asphaug 1994) or a hybrid SPH and N-body simulation (Leinhardt and Stewart 2009). This could validate the results of our modeling and provide clues on further improving the model.

A

Misalignment angle–angular momenta ratio dependence

Equation 3.11 defines the rotational axis misalignment angle after the collision. As we showed, it is closely related to the ratio of $L_{\mathrm{orb}}/L_{\mathrm{t}}$. Here we derive an approximate relation between these two quantities.

We assume that the shortest principal axis (represented by vector $\boldsymbol{E_3}$) of the target remains unchanged during the collision (the small deviation is caused by the crater formed on the body). We only consider the target rotational angular momentum $\boldsymbol{L_t}$ and the projectile orbital angular momentum $\boldsymbol{L_{\mathrm{orb,p}}}$ (further only $\boldsymbol{L_{\mathrm{orb}}}$ for simplicity) and neglect all other angular momenta in Eqn. 3.5, so the resulting $\boldsymbol{L^\star}$ is

$$\boldsymbol{L^\star} = \boldsymbol{L_{\mathrm{orb}}} + \boldsymbol{L_t}. \tag{A.1}$$

Hence we have

$$\cos\beta = \frac{\boldsymbol{L^\star}\boldsymbol{E_3}}{|\boldsymbol{L^\star}||\boldsymbol{E_3}|} = \frac{(\boldsymbol{L_{\mathrm{orb}}} + \boldsymbol{L_t})_z}{|\boldsymbol{L_{\mathrm{orb}}} + \boldsymbol{L_t}|}, \tag{A.2}$$

where the subscript z denotes the z component of the vector. This can be further

written as

$$\cos\beta = \frac{(L_{\text{orb}}\cos\psi + L_{\text{t}})}{[(L_{\text{orb}}\cos\psi + L_{\text{t}})^2 + L_{\text{orb}}^2\sin^2\psi]^{1/2}}\,, \tag{A.3}$$

where ψ is the angle between $\boldsymbol{L_{\text{orb}}}$ and $\boldsymbol{L_{\text{t}}}$ vectors. After some algebra we have

$$\cos\beta = \pm\left[1 + \frac{\sin^2\psi}{(L_{\text{t}}/L_{\text{orb}} + \cos\psi)^2}\right]^{-1/2}\,, \tag{A.4}$$

where the $+$ sign is for $L_{\text{t}} \geq -L_{\text{orb}}\cos\psi$ and $-$ sign is for $L_{\text{t}} < -L_{\text{orb}}\cos\psi$.

B

Limiting specific impact energy

Here we derive the limiting value of the specific impact energy Q^{tumb} as a function of physical parameters of the colliding bodies and the ratio of their angular momenta (orbital angular momentum of the projectile L_{orb} and the rotational angular momentum of the target before the collision L_{t}).

The ratio of the angular momenta is given by

$$\frac{L_{\text{t}}}{L_{\text{orb}}} = \frac{2\pi(a^2 + b^2)abc\rho}{5r_{\text{p}}^3 v_{\text{imp}}\delta P_{\text{t}}r_{\text{t}}}, \tag{B.1}$$

where v_{imp} is the impact speed, δ and ρ are the projectile and target density, respectively, r_{t} and r_{p} are their mean radii, respectively, a, b and c are the target's semi axes and P_{t} is the target's period of rotation. The specific energy of the collision in the system's centre of mass for $m_{\text{p}} \ll m_{\text{t}}$ is

$$Q = \frac{m_{\text{p}} v_{\text{imp}}^2}{2m_{\text{t}}} = \frac{r_{\text{p}}^3 v_{\text{imp}}^2 \delta}{abc\rho}, \tag{B.2}$$

m_{t} and m_{p} being the target and the projectile mass, respectively.

We solve Eqn. A.4 for L_t/L_{orb} ratio, Eqn. B.1 for r_p and insert both of them into Eqn. B.2. We then obtain the specific energy for which the tumbling starts to be apparent in the lightcurve

$$Q^{\text{tumb}} = \frac{\pi(a^2+b^2)v_{\text{imp}}}{5r_t P_t} \left(\frac{\sin^2 \psi}{\cos^{-2} \beta - 1} - \cos^2 \psi \right)^{-1}. \tag{B.3}$$

In Fig. 4.7 we use the derived value of $\beta = 15°$.

C

elwcrater documentation

The program used for the subcatastrophic collisions modeling is called `elwcrater` (ellipsoid with a crater). Here we describe its usage, input parameters, some hard-coded input limits and the produced outputs.

To run the program with default input, simply run the bash script `in.sh` which compiles the program with all necessary modules to the binary and runs it. The program calculates the circumstances of the collision and then generates the input for `do_lcs_free` program (by Josef Ďurech, see Appendix D). This program calculates the lightcurves and then some postprocessing is done.

C.1   Program input

The input parameters of the larger body (the target) are in set the `body.rc` file in the following way:

R[m] a/c b/c rho[kgm^{-3}] Y_bar[MPa] rot_period[h] kmax porosity

R is the mean radius of the body in meters, a/c and b/c are the semi-axis ratios (a>=b, c=1), rho is the body's mean density in $\mathrm{kg\,m^{-3}}$, Y_bar its material strength in MPa, rot_period is its initial rotation period in hours, kmax is the number of vertical segments of the body (the higher the better precision of the algorithm – set to couple hundreds to thousands depending on the machine you use to run the program), porosity (0 or 1) decides whether to consider the porosity of the body or not.

The impactor and crater parameters are set in the `crater.rc` file:

d[m] v_x v_y v_z[$\mathrm{m\,s^{-1}}$] phi theta[deg] delta[$\mathrm{kg\,m^{-3}}$] k1 k2 mju nu

d is the impactor diameter in meters, v_x, v_y and v_z are the x, y, z impact velocity components in $\mathrm{m\,s^{-1}}$, respectively, phi and theta are longitude and latitude of the impact point in degrees, respectively, delta is the impactor density in $\mathrm{kg\,m^{-3}}$, k1 and k2 are experiment-based coefficients and mju and nu are the scaling parameters (see Holsapple (2003); Holsapple (1993) and Holsapple and Housen 2007).

Spans of the input parameters

There are some limits of the input parameters caused either by physical reasoning, the usability of the scaling laws for impact crater dimensions calculation or by numerical constraints. Here we give those that are checked on the input by the program.

mean target radius: 1 m to R_{Earth}
a/c and b/c: < 4.2
rho: 800–6000 $\mathrm{kg\,m^{-3}}$
delta: 800–8000 $\mathrm{kg\,m^{-3}}$
impact speed: 1–72 $\mathrm{km\,s^{-1}}$
phi: 0–359 degrees
theta: -85–85 degrees (depending on the crater size, the crater cannot cross the pole)
impact angle: 0–50 degrees (the angle between the impact velocity vector and the line perpendicular to the surface at the impact point)

C.2 Program output

All the output files are saved to the `./vystupy/ID$id/` directory where $id is the unique number of the calculation run. The main output of the program is in the file `elwcrater.log`. It contains input parameters, various intermediate results, inertia tensor of the impacted body and β – the angle between the shortest principal axis and the angular momentum vector of the target after the collision. If the program finishes successfuly, the file contains `flag=0`, otherwise it is set to 1.

In the Appendix D, we present the documentation of `do_lcs_free` program we used for calculation of a lightcurve of the target body after the collision.

D

`do_lcs_free` documentation

Lightcurves of the post collision targets are generated by `do_lcs_free` program originally written by Mikko Kaasalainen (Kaasalainen 2001) and modified by Josef Ďurech (2011, pers. communication). The program calculates the total light flux scattered and reflected from the visible part of the asteroid model made by triangular facets. The initial orientation of rotational axis as well as the Euler angles that determine the body's orientation in space are given on the input. The Euler equations of motion are then solved and the integral light flux is calculated for given observational geometry with a chosen time increment.

D.1 Program input

There are two input files for a subroutine of `elwcrater` program which prepares the input for `do_lcs_free`. These are `lcpar.rc` and `geomlc.rc`. The former sets the parameters of the generated lightcurves and has the following structure:

number of lightcurves to be generated
the initial Julian day (the crater formation was just finished)
number of datapoints
time sampling in minutes of each lightcurve
sigma

The user is advised to let the sampling vary, so that accidental aliases with rotation/precession periods are overriden. One should not use too small sampling for many lightcurves (less than 1.5 minutes; it causes unknown numerical problems) and too much lightcurves (no more than nine). Sigma is a standard deviation of gaussian noise added to each lightcurve point (in percent of the mean flux).

The latter file contains orbit geometry parameters from JPL HORIZONS system (Yeomans 2013a; one can also use another ephemeris system) for five time instants. The program interpolates between them to generate all datapoints of the input lightcurve for `do_lcs_free`. Since the target body is hypothetical, the orbital geometry is, in fact, arbitrary. The structure of that input file is as follows:

Julian_day r hEcl-Lon hEcl-Lat delta ObsEcLon ObsEcLat

where Julian day (UT) gives the time instant, r is the heliocentric range of the asteroid (in AU), hEcl-Lon and hEcl-Lat are the heliocentric longitude and latitude of the asteroid, respectively, delta is the topocentric range (in AU), ObsEcLon and ObsEcLat are the topocentric longitude and latitude of the asteroid, respectively (all the angles are in degrees). We take those quantities from JPL HORIZONS system where they are given by 'Table Settings' 18–20, 29 and 31 and the date/time format is set to Julian day.

Body shape

The shape of the asteroid is given by the set of oriented triangles building up the body surface mesh. They are in the `*.tri` file in the following format:

n_ver n_fac
x y z
ver1 ver2 ver3

n_ver is the number of vertices and n_fac is the number of facets of the model, x, y and z are the cartezian coordinates of the vertices in the COM coordinate system and ver1, ver2 and ver3 is the ordering of the vertices making up the facet so that it is a triangle oriented by the outer normal vector (by right hand rule). The vertices and orderings are not interlaced in the file but all vertices are given first and then all orderings are given.

Dynamical parameters

The dynamical characteristics of the asteroid and the initial orientation in the ecliptic coordinate system are given in the `input` file as follows:

lambda beta
fi0 theta0 psi0
i1 i2 l
P_phi P_psi
jd0

where lambda and beta are the ecliptic longitude and latitude of the rotational axis, respectively, fi0, theta0 and psi0 are the Euler angles giving the initial orientation of the body in the space (all the angles are in degrees), i1 and i2 are the inertia moments normalized so that i3 = 1, l is normalized angular momentum (for unit volume of the body), P_phi and P_psi are the precession and rotation periods in hours (can be set to, say, one as an initial guess) and jd0 is the initial Julian day.

Scattering laws

The file `input_do_lcs` gives the scattering law parameters. There are two options, Hapke or Lommel–Seeliger + Lambert scattering. The first choice is given by five parameters, the second is given by two paraterers.

Input lightcurves

The input lightcurves contain ligtcurve data and orbital geometry of the asteroid in specific times. First, the number of lightcurves is given and then the lightcurves follow one after another. The first line of each lightcurve contains the number of

datapoints and the code discerning relative (0) and calibrated (1) lightcurve. After-
wards, each line of the lightcurve consists of the ligh time corrected Julian day, light
flux (reduced to unit distances from the Earth and the Sun when calibrated), the
ecliptic asteroid centric cartesian coordinates of the Sun and of the Earth in AU.

D.2   Program output

The main output is the lightcurve of the body just after the impact. The lightcurve
file `ID$id.lc` contains the geocentric Julian day, relative brightness of the body in
magnitudes, its uncertainty and the calculated light flux without the noise. There
is also a phasecurve generated with rotation period (`ID$id.ph`) which contains the
phase and the normalized light flux. Theoretical rotation and precession periods
are also calculated from dynamical characteristics of the body, see `periods.log`.
Besides, there is a `do_lcs_free.log` file and some scripts generating lightcurve
in fluxes rather than magnitudes and fitting trigonometric polynomial to the data
(`flux.sh`, `per.sh`).

E
List of publications

Papers

1. **Henych, T.**, Pravec, P., 2013. Asteroid rotation excitation by subcatastrophic impacts. MNRAS 432, 1623–1631.

2. Hanuš, J. et al. (including **T. Henych**), 2011. A study of asteroid pole-latitude distribution based on an extended set of shape models derived by the light-curve inversion method. A&A 530. A134, 16pp.

3. Pravec, P. et al. (including **T. Henych**), 2010. Formation of asteroid pairs by rotational fission. Nature 466. 1085–1088.

Conference proceedings

1. Scheeres, D. et al. (including **T. Henych**), 2010. Asteroid Pairs Formed by Rotational Fission. In: Bulletin of the American Astronomical Society, Division of Dynamical Astronomy Meeting #41. p. 926.

Abstracts of talks

1. **Henych, T.**, Pravec, P., June 2013. Asteroid rotation excitation by subcatas-
   trophic impacts. Contributed talk at 8th Workshop on Catastrophic disruption
   in the Solar System. Hawai'i, The Big Island, USA.

Bibliography

Benner, L. A. M., 2012. 2012 Goldstone Radar Observations of (4179) Toutatis. Accessed: 2013-07-30.
URL `http://echo.jpl.nasa.gov/asteroids/Toutatis2012/Toutatis2012_planning.html`

Benner, L. A. M., Ostro, S. J., Magri, C., Nolan, M. C., Howell, E. S., Giorgini, J. D., Jurgens, R. F., Margot, J.-L., Taylor, P. A., Busch, M. W., Shepard, M. K., 2008. Near-Earth asteroid surface roughness depends on compositional class. Icarus 198, 294–304.

Benz, W., Asphaug, E., 1994. Impact simulations with fracture. I - Method and tests. Icarus 107, 98.

Benz, W., Asphaug, E., 1999. Catastrophic Disruptions Revisited. Icarus 142, 5–20.

Binzel, R. P., A'Hearn, M., Asphaug, E., Barucci, M. A., Belton, M., Benz, W., Cellino, A., Festou, M. C., Fulchignoni, M., Harris, A. W., Rossi, A., Zuber, M. T., 2003. Interiors of small bodies: foundations and perspectives. Planet. Space Sci. 51, 443–454.

Black, G. J., Nicholson, P. D., Bottke, W. F., Burns, J. A., Harris, A. W., 1999. NOTE: On a Possible Rotation State of (433) Eros. Icarus 140, 239–242.

Bottke, W. F., Durda, D. D., Nesvorný, D., Jedicke, R., Morbidelli, A., Vokrouhlický, D., Levison, H. F., 2005. Linking the collisional history of the main asteroid belt to its dynamical excitation and depletion. Icarus 179, 63–94.

Bowell, E., Hapke, B., Domingue, D., Lumme, K., Peltoniemi, J., Harris, A. W., 1989. Application of photometric models to asteroids. In: Binzel, R. P., Gehrels, T., Matthews, M. S. (Eds.), Asteroids II. pp. 524–556.

Burchell, M. J., Leliwa-Kopystynski, J., 2010. The large crater on the small Asteroid (2867) Steins. Icarus 210, 707–712.

Burns, J. A., Safronov, V. S., 1973. Asteroid nutation angles. MNRAS 165, 403.

Chappelow, J. E., Sharpton, V. L., 2002. An improved shadow measurement technique for constraining the morphometry of simple impact craters. Meteoritics and Planetary Science 37, 479–486.

Chesley, S. R., 2006. Potential impact detection for Near-Earth asteroids: the case of 99942 Apophis (2004 MN 4). In: Daniela, L., Sylvio Ferraz, M., Angel, F. J. (Eds.), Asteroids, Comets, Meteors. Vol. 229 of IAU Symposium. pp. 215–228.

Descamps, P., et al., 2009. A giant crater on 90 Antiope? Icarus 203, 102–111.

Dobrovolskis, A. R., Burns, J. A., 1984. Angular momentum drain - A mechanism for despinning asteroids. Icarus 57, 464–476.

Donnison, J. R., Sugden, R. A., 1984. The distribution of asteroid diameters. MNRAS 210, 673–682.

Dunham, D. W., McFadden, L.-A., 1994. (253) Mathilde. IAU Circ. 6119, 2.

Efroimsky, M., Lazarian, A., 2000. Inelastic dissipation in wobbling asteroids and comets. MNRAS 311, 269–278.

Efroimsky, M., 2001. Relaxation of wobbling asteroids and comets-theoretical problems, perspectives of experimental observation. Planet. Space Sci. 49, 937–955.

Farnocchia, D., Chesley, S. R., Chodas, P. W., Micheli, M., Tholen, D. J., Milani, A., Elliott, G. T., Bernardi, F., 2013. Yarkovsky-driven impact risk analysis for asteroid (99942) Apophis. Icarus 224, 192–200.

Fujiwara, A., Kadono, T., Nakamura, A., 1993. Cratering experiments into curved surfaces and their implication for craters on small satellites. Icarus 105, 345.

Gauchez, D., Souchay, J., 2006. Simulation of post-impact rotational changes through multi-dimensional parametrization. Icarus 185, 83–96.

Giblin, I., Farinella, P., 1997. Tumbling Fragments from Experiments Simulating Asteroidal Catastrophic Disruption. Icarus 127, 424–430.

Harris, A. W., 1994. Tumbling asteroids. Icarus 107, 209.

Holsapple, K., Giblin, I., Housen, K., Nakamura, A., Ryan, E., 2002. Asteroid Impacts: Laboratory Experiments and Scaling Laws. Asteroids III , 443–462.

Holsapple, K. A., 1993. The scaling of impact processes in planetary sciences. Annual Review of Earth and Planetary Sciences 21, 333–373.

Holsapple, K. A., 1994. Catastrophic disruptions and cratering of solar system bodies: A review and new results. Planet. Space Sci. 42, 1067–1078.

Holsapple, K. A., 2003. Theory and equations for 'Craters from Impacts and Explosions'. Accessed: 2011-11-01.
URL `http://keith.aa.washington.edu/craterdata/scaling/theory.pdf`

Holsapple, K. A., 2007. Spin limits of Solar System bodies: From the small fast-rotators to 2003 EL61. Icarus 187, 500–509.

Holsapple, K. A., Housen, K. R., 2007. A crater and its ejecta: An interpretation of Deep Impact. Icarus 187, 345–356.

Holsapple, K. A., Housen, K. R., 2012a. Momentum transfer in asteroid impacts. I. Theory and scaling. Icarus 221, 875–887.

Holsapple, K. A., Housen, K. R., 2012b. Studies of Impacts: Experimental and Numerical Simulations of Cratering, Disruptions and Asteroid Deflections. LPI Contributions 1667, 6367.

Holsapple, K. A., Schmidt, R. M., 1987. Point source solutions and coupling parameters in cratering mechanics. J. Geophys. Res. 92, 6350–6376.

Housen, K., 2009. Cumulative damage in strength-dominated collisions of rocky asteroids: Rubble piles and brick piles. Planet. Space Sci. 57, 142–153.

Housen, K. R., 2004. Collisional Fragmentation of Rotating Bodies. In: Mackwell, S., Stansbery, E. (Eds.), Lunar and Planetary Institute Science Conference Abstracts. Vol. 35 of Lunar and Planetary Inst. Technical Report. p. 1826.

Housen, K. R., Holsapple, K. A., 2003. Impact cratering on porous asteroids. Icarus 163, 102–119.

Housen, K. R., Holsapple, K. A., 2011. Ejecta from impact craters. Icarus 211, 856–875.

Housen, K. R., Holsapple, K. A., 2012. Deflecting Asteroids by Impacts: What is Beta? In: Lunar and Planetary Institute Science Conference Abstracts. Vol. 43 of Lunar and Planetary Institute Science Conference Abstracts. p. 2539.

Housen, K. R., Holsapple, K. A., Voss, M. E., 1999. Compaction as the origin of the unusual craters on the asteroid Mathilde. Nature 402, 155–157.

Hudson, R. S., Ostro, S. J., 1995. Shape and Non-Principal Axis Spin State of Asteroid 4179 Toutatis. Science 270, 84–86.

Hudson, R. S., Ostro, S. J., Scheeres, D. J., 2003. High-resolution model of Asteroid 4179 Toutatis. Icarus 161, 346–355.

Ivezić, Ž., et al., 2001. Solar System Objects Observed in the Sloan Digital Sky Survey Commissioning Data. AJ 122, 2749–2784.

Jenniskens, P., et al., 2009. The impact and recovery of asteroid 2008 TC$_3$. Nature 458, 485–488.

Kaasalainen, M., 2001. Interpretation of lightcurves of precessing asteroids. A&A 376, 302–309.

Kopal, Z., 1970. The Axial Rotation of Asteroids. Ap&SS 6, 33–35.

Kryszczyńska, A., Kwiatkowski, T., Breiter, S., Michałowski, T., 1999. Relation between rotation and lightcurve of 4179 Toutatis. A&A 345, 643–645.

Kvasnica, J., 1997. Matematický aparát fyziky. Academia, Prague, Mathematical tools of Physics, in Czech.

Landau, L. D., Lifshitz, E. M., 1976. Mechanics. Butterworth-Heinemann, Oxford.

Leinhardt, Z. M., Stewart, S. T., 2009. Full numerical simulations of catastrophic small body collisions. Icarus 199, 542–559.

Leinhardt, Z. M., Stewart, S. T., 2012. Collisions between Gravity-dominated Bodies. I. Outcome Regimes and Scaling Laws. ApJ 745, 79.

Leliwa-Kopystyński, J., Burchell, M. J., Lowen, D., 2008. Impact cratering and break up of the small bodies of the Solar System. Icarus 195, 817–826.

Love, S. G., Ahrens, T. J., 1996. Catastrophic Impacts on Gravity Dominated Asteroids. Icarus 124, 141–155.

Macháček, D., 2012. Composite image of Toutatis from Chang'E 2 photos. Accessed: 2013-05-24.
URL http://www.planetary.org/multimedia/space-images/small-bodies/composite-image-of-toutatis.html

Marsden, B. G., 1989. IAUC 4701: 1989b; 1989 AC; 1987g. Accessed: 2013-05-27.
URL http://www.cbat.eps.harvard.edu/iauc/04700/04701.html#Item2

Marzari, F., Rossi, A., Scheeres, D. J., 2011. Combined effect of YORP and collisions on the rotation rate of small Main Belt asteroids. Icarus 214, 622–631.

Molina, A., Moreno, F., Martinez-López, F., 2003. Energy dissipation by internal stresses in a free-rotating symmetric ellipsoid: Application to Comet P/Halley. A&A 398, 809–817.

Mottola, S., et al., 1995. The slow rotation of 253 Mathilde. Planet. Space Sci. 43, 1609–1613.

Mueller, B. E. A., Samarasinha, N. H., Belton, M. J. S., 2002. The Diagnosis of Complex Rotation in the Lightcurve of 4179 Toutatis and Potential Applications to Other Asteroids and Bare Cometary Nuclei. Icarus 158, 305–311.

Nolan, M. C., Asphaug, E., Melosh, H. J., Greenberg, R., 1996. Impact Craters on Asteroids: Does Gravity or Strength Control Their Size? Icarus 124, 359–371.

Noll, K. S., Weaver, H. A., Storrs, A. D., Zellner, B., 1995. Imaging of Asteroid 4179 Toutatis with Hubble Space Telescope. Icarus 113, 353–359.

Ostro, S. J., Hudson, R. S., Rosema, K. D., Giorgini, J. D., Jurgens, R. F., Yeomans, D. K., Chodas, P. W., Winkler, R., Rose, R., Choate, D., Cormier, R. A., Kelley, D.,

Littlefair, R., Benner, L. A. M., Thomas, M. L., Slade, M. A., 1999. Asteroid 4179 Toutatis: 1996 Radar Observations. Icarus 137, 122–139.

Ostro, S. J., et al., 1995. Radar Images of Asteroid 4179 Toutatis. Science 270, 80–83.

Paddack, S. J., 1969. Rotational burning of scmall celestial bodies: Effects of radiation pressure. J. Geophys. Res. 74, 4379–4381.

Paolicchi, P., Burns, J. A., Weidenschilling, S. J., 2002. Side Effects of Collisions: Spin Rate Changes, Tumbling Rotation States, and Binary Asteroids. Asteroids III , 517–526.

Peale, S. J., Lissauer, J. J., 1989. Rotation of Halley's comet. Icarus 79, 396–430.

Pravec, P., Hahn, G., 1997. Two-Period Lightcurve of 1994 AW_1: Indication of a Binary Asteroid? Icarus 127, 431–440.

Pravec, P., Harris, A. W., 2000. Fast and Slow Rotation of Asteroids. Icarus 148, 12–20.

Pravec, P., Hergenrother, C., Whiteley, R., Šarounová, L., Kušnirák, P, Wolf, M., 2000. Fast Rotating Asteroids 1999 TY_2, 1999 SF_{10}, and 1998 WB_2. Icarus 147, 477–486.

Pravec, P., et al., 2005. Tumbling asteroids. Icarus 173, 108–131.

Richardson, D. C., Bottke, W. F., Love, S. G., 1998. Tidal Distortion and Disruption of Earth-Crossing Asteroids. Icarus 134, 47–76.

Richardson, J. E., 2009. Cratering saturation and equilibrium: A new model looks at an old problem. Icarus 204, 697–715.

Rubincam, D. P., 2000. Radiative Spin-up and Spin-down of Small Asteroids. Icarus 148, 2–11.

Samarasinha, N. H., A'Hearn, M. F., 1991. Observational and dynamical constraints on the rotation of Comet P/Halley. Icarus 93, 194–225.

Scheeres, D. J., Ostro, S. J., Werner, R. A., Asphaug, E., Hudson, R. S., 2000. Effects of Gravitational Interactions on Asteroid Spin States. Icarus 147, 106–118.

Scheirich, P., et al., 2010. The shape and rotation of asteroid 2008 TC_3. Meteoritics and Planetary Science 45, 1804–1811.

Sharma, I., Burns, J. A., Hui, C.-Y., 2005. Nutational damping times in solids of rev-
olution. MNRAS 359, 79–92.

Spencer, J. R., et al., 1995. The lightcurve of 4179 Toutatis: Evidence for complex
rotation. Icarus 117, 71–89.

Statler, T. S., 2009. Extreme sensitivity of the YORP effect to small-scale topography.
Icarus 202, 502–513.

Stewart, S. T., Leinhardt, Z. M., 2009. Velocity-Dependent Catastrophic Disruption
Criteria for Planetesimals. ApJ 691, L133–L137.

Stewart, S. T., Leinhardt, Z. M., 2012. Collisions between Gravity-dominated Bodies.
II. The Diversity of Impact Outcomes during the End Stage of Planet Formation.
ApJ 751, 32.

Takeda, T., Ohtsuki, K., 2009. Mass dispersal and angular momentum transfer dur-
ing collisions between rubble-pile asteroids. II. Effects of initial rotation and spin-
down through disruptive collisions. Icarus 202, 514–524.

Thomas, P. C., 1999. Large Craters on Small Objects: Occurrence, Morphology, and
Effects. Icarus 142, 89–96.

Thomas, P. C., Veverka, J., Bell, J. F., Clark, B. E., Carcich, B., Joseph, J., Robinson,
M., McFadden, L. A., Malin, M. C., Chapman, C. R., Merline, W., Murchie, S., 1999.
Mathilde: Size, Shape, and Geology. Icarus 140, 17–27.

Tonon, F., 2004. Explicit Exact Formulas for the 3-D Tetrahedron Inertia Tensor in
Terms of its Vertex Coordinates. J. Math. Stat. 1, 8–11.

Varnes, E., 2004. Physics 321 lecture notes (fall 2004). Accessed: 2013-05-02.
URL   `http://www.physics.arizona.edu/~varnes/Teaching/`
`321Fall2004/Notes/index.html`

Veverka, J., et al., 1999. NEAR Encounter with Asteroid 253 Mathilde: Overview.
Icarus 140, 3–16.

Veverka, J., Thomas, P., Harch, A., Clark, B., Bell, III, J. F., Carcich, B., Joseph, J., Chap-
man, C., 1997. NEAR's Flyby of 253 Mathilde: Images of a C Asteroid. Science 278,
2109.

Vokrouhlický, D., Breiter, S., Nesvorný, D., Bottke, W. F., 2007. Generalized YORP evolution: Onset of tumbling and new asymptotic states. Icarus 191, 636–650.

Walker, J. D., Chocron, S., Durda, D. D., Grosch, D. J., Movshovitz, N., Richardson, D. C., Asphaug, E., 2012. Momentum enhancement from aluminum striking granite and the scale size effect. International Journal of Impact Engineering .

Yanagisawa, M., 2002. Collisional Spin Up of Nonspherical Asteroids. Icarus 159, 300–305.

Yanagisawa, M., Hasegawa, S., 2000. Momentum Transfer in Oblique Impacts: Implications for Asteroid Rotations. Icarus 146, 270–288.

Yanagisawa, M., Hasegawa, S., Shirogane, N., 1996. Momentum and Angular Momentum Transfer in Oblique Impacts: Implications for Asteroid Rotations. Icarus 123, 192–206.

Yeomans, D. K., 2013a. JPL HORIZONS system web-based interface. Accessed: 2013-08-16.
   URL http://ssd.jpl.nasa.gov/horizons.cgi

Yeomans, D. K., 2013b. JPL Small-Body Database Browser. Accessed: 2013-07-30.
   URL   http://ssd.jpl.nasa.gov/sbdb.cgi?sstr=toutatis;orb=0;
   cov=0;log=0;cad=0#discovery

Yeomans, D. K., 2013c. JPL Small-Body Database Browser. Accessed: 2013-08-08.
   URL   http://ssd.jpl.nasa.gov/sbdb.cgi?sstr=mathilde;orb=0;
   cov=0;log=0;cad=0#discovery

Yeomans, D. K., 2013d. JPL Small-Body Database Browser. Accessed: 2013-08-08.
   URL   http://ssd.jpl.nasa.gov/sbdb.cgi?sstr=apophis;orb=0;
   cov=0;log=0;cad=0#discovery

Yeomans, D. K., Scheeres, D. J., Konopliv, A. S., Giorgini, J. D., Chodas, P. W., Chamberlin, A. B., Barriot, J.-P., 1997. The Mass of Asteroid 253 Mathilde from near Tracking Data. In: AAS/Division for Planetary Sciences Meeting Abstracts #29. Vol. 29 of Bulletin of the American Astronomical Society. p. 972.

The thesis has been typeset with TeX and LaTeX.